We are IntechOpen, the world's leading publisher of Open Access books Built by scientists, for scientists

6,900
Open access books available

185,000
International authors and editors

200M
Downloads

Our authors are among the

154
Countries delivered to

TOP 1%
most cited scientists

12.2%
Contributors from top 500 universities



WEB OF SCIENCE™

Selection of our books indexed in the Book Citation Index in Web of Science™ Core Collection (BKCI)

Interested in publishing with us?
Contact book.department@intechopen.com

Numbers displayed above are based on latest data collected.
For more information visit www.intechopen.com



10

Rate-Dependent Nonlinear Seismic Response Analysis of Concrete Arch Dam

Xiao Shiyun
Faculty of Infrastructure Engineering, Dalian University of Technology, Dalian, China

1. Introduction

In civil engineering, all kinds of concrete structures inevitably encounter some form of dynamic loading during their lifetime. For example, bridges and tall buildings encounter wind loading, dams suffer from hydrodynamic pressure loading, ocean platforms encounter the impact of ocean waves, and all kinds of structures may suffer from earthquake loading. Because of their unpredictability and destructive capacity, these kinds of loadings always become important factors in controlling structural design.

The concrete is a typical rate-dependent material: its strength, stiffness, and ductility (or brittleness) are affected by loading rates. Researches on the rate dependency of concrete started in 1917 by the Abrams' dynamic compressive experiment (Abrams 1917). Jones (1936) investigated the relationship between compressive strengths of concrete and loading rates. Their experiments gave the conclusion that the compressive strengths of concrete increased with loading rates. Numerous tests have been carried out to investigate the response of concrete to rapid loading. Watstein (1953) observed that the compressive strengths of concrete increased an average of 80 percent when the strain rate increased from the static loading rate $10^{-6}s^{-1}$ to $10s^{-1}$. Based on the results of his experiments, Norris (1959) proposed an empirical formula and predicted that the compressive strengths were increased up to 33%, 24%, and 17% greater than the static strengths when the strain rates were $3s^{-1}$, $0.3s^{-1}$, and $0.1s^{-1}$, respectively. Atchley (1967) reported that the dynamic compressive strength increased from 25% to 38%. Experimental results from Hughes (1972) illustrated that the compressive strengths of concrete increased 90% more than the static strength on the impact loading.

Although researchers are not in complete agreement with which strain rates cause the increase in strength to be significant, it is generally accepted that a definite increase in the uniaxial compressive strength of concrete correlates with the increase of strain rates. However, confusion also has arisen in regard to the increase in magnitude of dynamic strengths. Some experimental results (Abrams 1917; Jones 1936; Watstein 1953; Rush 1960; Atchley 1967; Spooner 1972; Hughes 1972; Sparks 1973; Dilger 1984) showed that an increase of 30 percent more than the static strength of concrete, and even up to 80 percent, is possible. Others, such as Moore (1934), Evans (1942) and Dhir (1972), indicated that the increase in the strength of concrete was less than 20 percent and was not influenced by the rate of loading. Bischoff (1991) reviewed and analyzed the dynamic compressive experiments of concrete and deduced that the confusion about the increased magnitude of dynamic strengths arose

because many factors, such as concrete quality, aggregate, age, curing and moisture conditions, influenced the behavior during the rapid loading.

The reported dynamic tensile tests of concrete in literature are more difficult to perform and the results are few. Birkimer (1971) conducted two sets of dynamic tensile tests using plain concrete cylinders. In the first set, the dynamic strength at the strain rate of $20s^{-1}$ was between 17.2 MPa and 22.1 MPa, whereas the static tensile strength was 3.4 MPa at the quasi-static strain rate of $0.57\times10^{-6}s^{-1}$. In the second set, the concrete dynamic strength was between 15.4 MPa and 27.6 MPa. Zielinski (1981) studied the behavior of concrete subjected to the uniaxial impact tensile loading and found that the ratios of impact and static tensile strengths were between 1.33 and 2.34 for various concrete mixes. Oh (1987) presented a realistic nonlinear stress-strain model that could describe the dynamic tensile behavior of concrete. An equation was proposed to predict the increase of tensile strengths resulting from an increase of strain rate. Tedesco (1991) conducted the direct tension tests of plain concrete specimens on a split-Hopkinson pressure bar to investigate the effects of increasing strain rate on the tensile strength of concrete. Rossi (1994) made an experimental study of rate effects on the behaviors of concrete under tensile stress to investigate the effect of the water/cement ratio on the tensile strength enhancement. In addition, an analysis of the physical mechanisms was developed to investigate how the Stefan effect, the cracking process, and the inertia forces participated together in the dynamic behavior of a specimen subjected to a uniaxial tensile test (Rossi, 1996). Cadoni (2001) studied the effect of strain rate on the tensile behavior of concrete at different relative humidity levels. Malvar (1998) reviewed the extant data characterizing the effects of strain rate on the tensile strength of concrete and compared the DIF formulation with that recommended by the European CEB. Finally, an alternative formulation was proposed based on the experimental data.

Many high arch dams have been built and will be built in areas of China with high seismic activity. Some of them will reach 300 meters in height. For researchers and engineers, the significant concern is paid on the safety of these structures against earthquake shocks. During the past two or three decades, many sophisticated computer programs are developed and used for numerical analysis of the arch dams. Our ability to analyze mathematical models of dam structures subjected to earthquake ground motions has been improved dramatically. Nevertheless, the current design practice in the seismic design of arch dams has to be based on the linear elastic assumption. The key property that determines the capacity of arch dams to withstand earthquakes is the tensile strength of concrete. However, the design criterion for the tensile stress remained a problem at issue. A widely accepted standard has not been available. The conventional design practice accounts for the rate sensitivity by means of drastic simplifying assumptions. That is, in all cases, the allowable stresses of an arch dam under earthquake load are increased by, such as a Chinese Standard (2001), 30% of the value specified for static case. Similarly, the dynamic modulus of elasticity is assigned 30% higher than its static value. Raphael (1984) carried out the dynamic test of concrete from dam cores and reported an average dynamic-static splitting tensile strength ratio of 1.45, and an average dynamic-static compressive strength ratio of 1.31 for the same loading rate ranges. Harris (2000) performed laboratory tests on concrete cores drilled from dams and tested at strain rates that simulated dynamic and static loading conditions. Results indicated that dynamic-static strength ratios were greater than those for both the tensile and compressive strength tests. Thereby, it is improper that the same increments of strengths and elastic modulus of concrete at different strain rates are adopted during the process of analyzing the seismic response of dams.

Few researchers considered the effect of strain rates on dynamic responses of arch dams because there was a lack of rate-dependent dynamic constitutive models of concrete. Cervera (1996) developed a rate-dependent isotropic damage model for the numerical analysis of concrete dams. The application of the proposed model to the seismic analysis of a large gravity concrete dam showed that the tensile peak strength of concrete could be increased up to 50 percent for the range of strain rates that appear in a structural safety analysis of a dam subjected to severe seismic actions. Lee (1998) developed a plastic-damage model for the concrete subjected to cyclic loading using concepts of fracture-energy-based damage and stiffness degradation. The rate-dependent regularization was used to guarantee a unique converged solution for softening regions. No effect for the rate-dependency on the stress distribution has been involved. Chen (2004) proposed a rate-dependent damage constitutive model for massive concrete by introducing rate-dependant plastic damage variables as internal variables. The nonlinear seismic responses of arch dams were computed using this model and the results were compared with the results given by the corresponding rate-independent damage model. It showed that the distribution of strain rates not only influenced the vibration modes of dam but also had significant effects on the dynamic damage of arch dams. Li (2005) analyzed the seismic response of a high arch dam, in which a rate-dependent damage constitutive model of concrete was considered and the nonlinear contact of joints was simulated by direct stiffness method based on the Lagrange multiplier. The study showed that the nonlinear concrete model had great effects on the dynamic opening of the contraction joints caused by the nonlinear softening and cracking. Bai (2006) established a rate-dependent damage constitutive model for simulating the mechanical behaviors of concrete by introducing the effect of strain rate into the damage tensor. The model was applied to analyze the seismic overload response of a typical concrete gravity dam. Results indicated that the distribution of strain rate caused by seismic loading varied at the dam surface and significantly affected the dynamic response.

The effect of strain rates on dynamic behaviors of concrete is an important aspect in the evaluation of the seismic responses of concrete structures. To evaluate the seismic behaviors of concrete structures, the dynamic experiment and the dynamic constitutive model of concrete are necessary. The main objective of this study is, based on the results of the dynamic uniaxial tensile and compressive experiments on the concrete, to establish the dynamic constitutive model of concrete and study the effect of strain rates on dynamic responses of concrete dams.

2. Dynamic experiments of concrete

2.1 Dynamic uniaxial tensile experiment of concrete

2.1.1 Tensile specimen

A concrete mix with proportions, by weight, of cement: water: gravel: sand content = 1.00:0.75:4.09:2.56 was used in the study. The employed cement is 425 Portland cement, the fine aggregate is general river sand, and the coarse aggregate is crushed rock. Specimens were cast in steel moulds and cured in moisture condition for 7 days, then they were naturally cured at 20±3 Celsius degree temperature in the laboratory. Fifty dumbbell-shaped specimens were cast for the tensile experiment, as shown in **Fig.1**. The specimens of dumbbell shape ensure that the specimens were destroyed at the middle of specimen in tension.

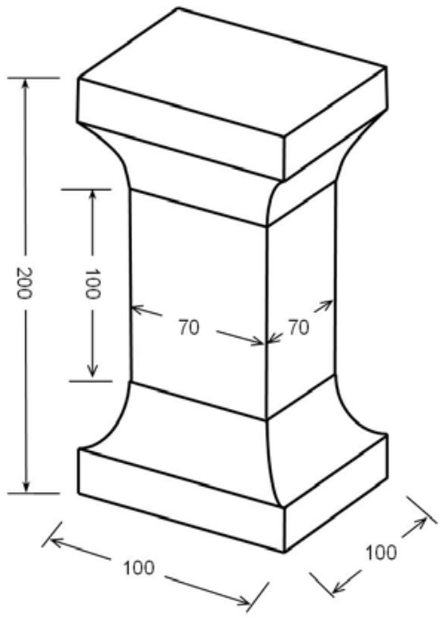


Fig. 1. Tensile specimen

2.1.2 Tensile test loading system and measuring system

The tensile dynamic test was carried out using the 1000-kN servo fatigue testing machine at the State Key Laboratory of Coastal and Offshore, Dalian University of Technology. During the process of experiments, the loading sign is sent by the control center, and then it is transferred to the servo fatigue testing machine. The magnitude and frequencies of loading are controlled by the control center.

During the tensile test, the specimen was adhered to two steel plates by the constructional glue. The bottom steel plate was fixed to the base with bolts and the upper steel plate was connected to the load cell with the load transducer, as shown in **Fig. 2**. In order to increase the stiffness of the loading system, a frame was formed by four steel bars connecting the load cell to the base with bolts.



Fig. 2. Tensile test setup

The data acquisition processor is 32-channel. Vertical and lateral strains of specimens were measured by four pairs of decussate strain gauges adhered on the four sides of specimens. Vertical and lateral displacements were measured by two opposite Linear Variable Displacement Transducers (LVDT) fixed to two opposite sides of the specimen. The load was measured by the load transducer fixed to the specimen. All measured signals were transmitted to the data acquisition and processing system of the computer through a specially allocated amplifier.

2.1.3 Analysis of the tensile experimental results

2.1.3.1 Stain-rate influence on uniaxial strength of concrete

The dynamic tensile strengths of 15 specimens under different strain rates of $10^{-5}s^{-1}$, $10^{-4}s^{-1}$, $10^{-3}s^{-1}$and $10^{-2}s^{-1}$ are shown in **table 1**. It shows that the uniaxial tensile strengths of concrete increase with the increasing of strain rates. Compared to the quasi-static tensile strength of concrete at the strain rate of $10^{-5}s^{-1}$, the dynamic tensile strengths of concrete at strain rates of $10^{-4}s^{-1}$, $10^{-3}s^{-1}$ and $10^{-2}s^{-1}$ increase 6%, 10% and 18%, respectively.

Strain rate / s^{-1}	Tensile Strengths / MPa			
	10^{-5}	10^{-4}	10^{-3}	10^{-2}
1	1.388	1.435	1.549	1.639
2	1.582	1.480	1.502	1.753
3	1.469	1.604	1.696	1.731
4	1.355	1.606	1.629	
average	1.449	1.531	1.594	1.696

Table 1. Dynamic strength of concrete in tension

According to the references, the increases in strengths follow a linear-logarithmic relationship with the increases in strain rates. By test results the linear-logarithmic relationship between the tensile strength enhancement with the strain rate enhancement, is given by

$$f_t / f_{ts} = 1.0 + 0.057 \log\left(\dot{\varepsilon}_t / \dot{\varepsilon}_{ts}\right) \tag{1}$$

Fig.3 shows the relationship between the dynamic tensile strength and the static tensile strength of concrete at different strain rates of $10^{-5}s^{-1}$, $10^{-4}s^{-1}$, $10^{-3}s^{-1}$and $10^{-2}s^{-1}$.

2.1.3.2 Stain-rate influence on elastic modulus

The stress-strain curves of concrete in tension at different strain-rate loading are illustrated in **Fig.4**. It is clear that during different strain rate loading the slope of curves is linear at the beginning of loading, indicating that the initial tangent modulus of concrete is independent of strain rate.

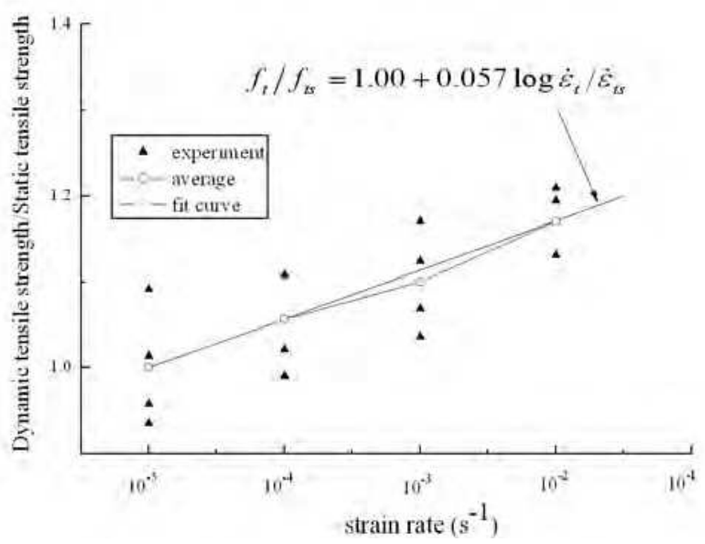


Fig. 3. The relationship between the dynamic tensile strength and the static tensile strength

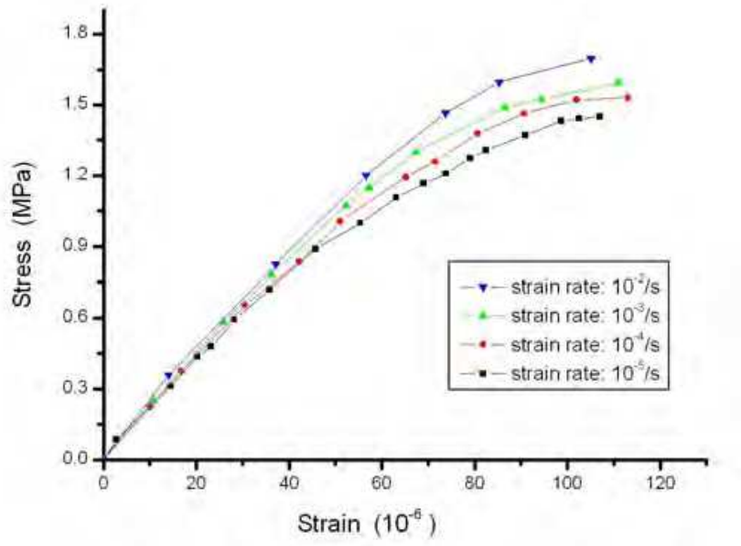


Fig. 4. The stress-strain curves of concrete in tension

2.1.3.3 Stain-rate influence on critical strain

Table 2 illustrates the critical strain of concrete in tension obtained from the present test. **Table 2** implies that in the range of strain rate from $10^{-5}s^{-1}$ to $10^{-2}s^{-1}$, the effect of strain rate on the critical strain value of concrete in tension is little, if any.

Strain rate	$10^{-5}s^{-1}$	10^{-4} s^{-1}	10^{-3} s^{-1}	10^{-2} s^{-1}
1	106	106	122	102
2	127	130	98	114
3	113	112	108	123
4	102	114	110	
Average	112	116	110	113

Table 2. The critical strain of concrete in tension

2.1.3.4 Stain-rate influence on Poisson's ratio

Table 3 shows the change in Poisson's ratio of concrete in tension and compression. It is found that the maximum of Poisson's ratio is 0.20 but the minimum is 0.13. And it is concluded that Poisson's ratio isn't obviously dependent on the loading rate according to the average of results.

Strain rate	$10^{-5}s^{-1}$	10^{-4} s^{-1}	10^{-3} s^{-1}	10^{-2} s^{-1}
1	0.16	0.17	0.14	0.15
2	0.14	0.16	0.14	0.19
3	0.19	0.18	0.15	0.13
4	0.14	0.13	0.16	
Average	0.16	0.16	0.15	0.16

Table 3. The Poisson's ratio of concrete in tension

2.2 Dynamic uniaxial compressive experiment of concrete

2.2.1 Compressive specimen

Similar to the tensile specimen, the concrete mix with proportions, by weight, of cement: water: gravel: sand content was still 1.00:0.75:4.09:2.56. The employed cement is 425 Portland cement, the fine aggregate is general river sand, and the coarse aggregate is crushed rock. Specimens were cast in steel moulds and cured in moisture condition for 7 days, then they were naturally cured at 20±3 Celsius degree temperature in the laboratory. Fifty cuboid specimens with 100×100×300mm were cast for the compressive experiment, as shown in **Fig.5**.

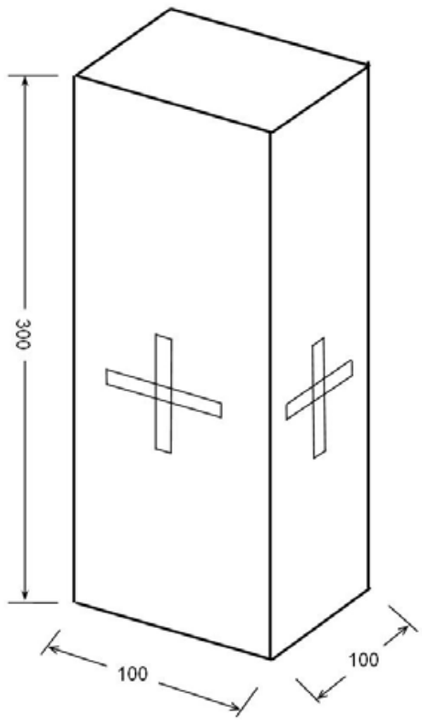


Fig. 5. Compressive specimen

2.2.2 Compressive test loading system and measuring system

The compressive dynamic test was also carried out using the 1000-kN servo fatigue testing machine at the State Key Laboratory of Coastal and Offshore, Dalian University of Technology. As for the compressive test, the cuboid specimen was placed vertically on the circular steel plate connecting the base with the load transducer, as shown in **Fig. 6**. The measure system is same as the tensile test.



Fig. 6. Compressive test setup

2.2.3 Analysis of the compressive experimental results

2.2.3.1 Stain-rate influence on uniaxial strength of concrete

Table 4 gives the dynamic compressive strengths of concrete at different strain rates. It can be concluded that the uniaxial compressive strengths of concrete increase with the increasing of strain rate. Compared to the quasi-static compressive strength of concrete at the strain rate of $10^{-5}s^{-1}$, the dynamic compressive strengths of concrete at strain rate of $10^{-4}s^{-1}$, $10^{-3}s^{-1}$, $10^{-2}s^{-1}$ and $10^{-1}s^{-1}$ increase 4.8%, 9.0%, 12.0% and 15.6%, respectively.

Strain rate / s^{-1}	Compressive strengths / MPa				
	10^{-5}	10^{-4}	10^{-3}	10^{-2}	10^{-1}
1	21.89	22.09	24.63	24.04	26.19
2	22.03	24.40	23.18	25.97	24.94
3	20.67	21.72	22.60	22.70	26.72
4	23.35	23.93	25.44	25.76	23.76
average	22.00	23.03	23.96	24.62	25.40

Table 4. Dynamic strengths of concrete in compression

Similar to the dynamic tensile strength, the linear-logarithmic relationship between the compressive strength enhancement with the strain rate enhancement, is also given by

$$f_c / f_{cs} = 1.0 + 0.040 \log\left(\dot{\varepsilon}_c / \dot{\varepsilon}_{cs}\right) \tag{2}$$

Fig.7 gives the relationship between the dynamic compressive strength and the static compressive strengths of concrete.

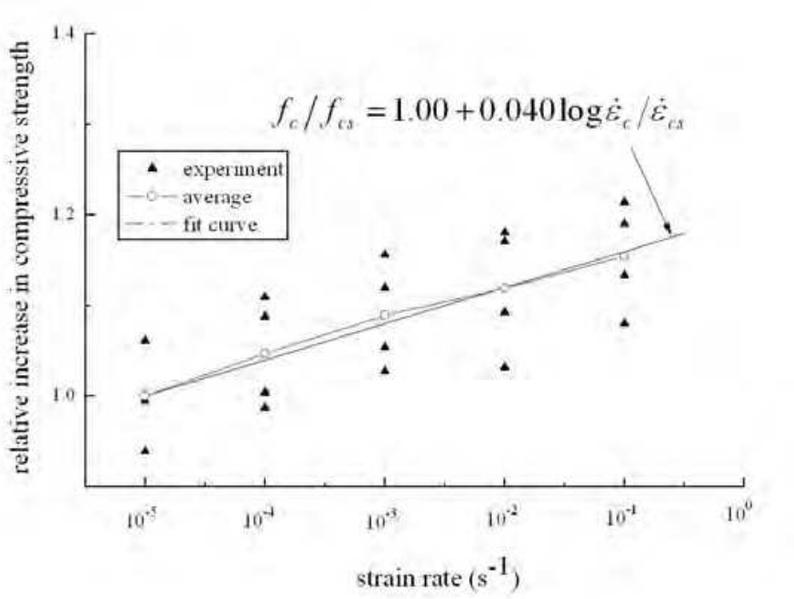


Fig. 7. The relationship between the dynamic and static compressive strength

2.2.3.2 Stain-rate influence on elastic modulus

The stress-strain curves of concrete in compression at different strain-rate loading are plotted in **Fig.8**. The initial tangent modulus of concrete in compression slightly increased as the strain rate increased. The initial tangent moduli of concrete at strain rate of $10^{-4}s^{-1}$, $10^{-3}s^{-1}$, $10^{-2}s^{-1}$ and $10^{-1}s^{-1}$ increase to 1.3×10^{4}MPa, 1.38×10^{4}MPa, 1.48×10^{4}MPa and 1.60×10^{4}MPa from 1.23×10^{4}MPa at strain rate of $10^{-5}s^{-1}$, respectively.

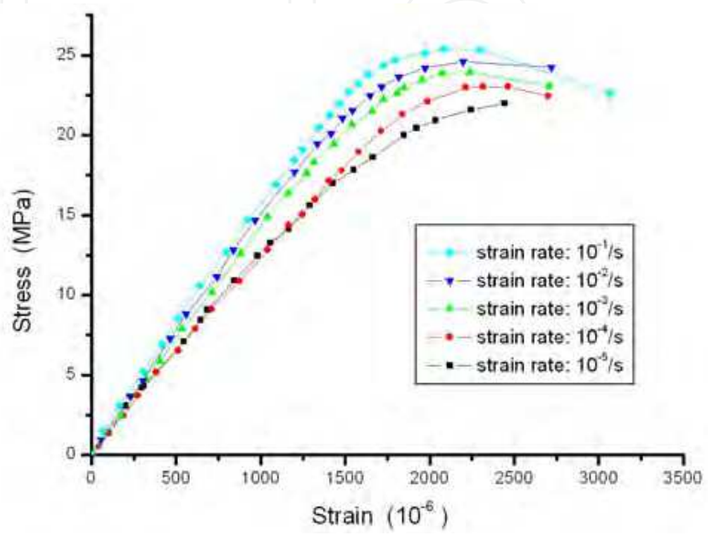


Fig. 8. The stress-strain curves of concrete in compression

2.2.3.3 Stain-rate influence on critical strain

Table 5 gives the results of the critical compressive strain of concrete obtained from the present test. It shows that a slight decrease in the critical compressive strain value was observed as the strain rate was increased.

Strain rate	$10^{-5}s^{-1}$	10^{-4} s^{-1}	10^{-3} s^{-1}	10^{-2} s^{-1}	10^{-1} s^{-1}
1	2524	2164	2480	2382	2030
2	2713	2153	2244	2172	2114
3	2180	2633	2083	2231	2234
4	2353	2304	2137	2003	1965
Average	2443	2314	2236	2197	2086

Table 5. The critical strain of concrete in compression

2.2.3.4 Stain-rate influence on Poisson's ratio

Table 6 shows the change in Poisson's ratio of concrete in tension and compression. It is found that the maximum of Poisson's ratio is 0.20 but the minimum is 0.13. And it is concluded that Poisson's ratio isn't obviously dependent on the loading rate according to the average of results.

Strain rate	$10^{-5}s^{-1}$	10^{-4} s^{-1}	10^{-3} s^{-1}	10^{-2} s^{-1}	10^{-1} s^{-1}
1	0.18	0.14	0.20	0.14	0.15
2	0.13	0.19	0.18	0.18	0.17
3	0.15	0.16	0.14	0.17	0.17
4	0.17	0.15	0.17	0.20	0.15
Average	0.16	0.16	0.17	0.17	0.16

Table 6. The Poisson's ratio of concrete in compression

3. Rate-dependent constitutive model of concrete

3.1 Consistency viscoplastic model theory

The consistency viscoplastic model can be seen as an extension of the classic elasto-plastic model to account for the rate-dependent behavior of materials. This model, which uses the Von Mises yield surface, was applied by Wang (1997) to analyze metal. With this method, the consistency viscoplastic Hoffman model of concrete was modified by Winnicki (2001). In this model, during viscoplastic flow, the actual stress state must remain on the yield surface, and the consistency condition is imposed.

The viscoplastic yield function can be expressed as

$$F(\sigma_{ij},\kappa,\dot{\kappa})=0 \quad \text{for } \dot{\lambda}>0 \tag{3}$$

In uniaxial tension and compression, equation (3) can be expressed as

$$\left.\begin{aligned} F_c &= F(\sigma_{ij},\kappa_c,\dot{\kappa}_c)\\ F_t &= F(\sigma_{ij},\kappa_t,\dot{\kappa}_t)\end{aligned}\right\} \tag{4}$$

It is difficult to establish biaxial or triaxial constitution relations because of the lack of biaxial dynamic experiment results for the concrete. For simplicity, the biaxial dynamic behavior of concrete is assumed to be the same as the uniaxial dynamic behavior with an increasing factor K_{bc} for the strength such that:

$$f_{bc}=K_{bc}f(\sigma_{ij},\kappa_c,\dot{\kappa}_c) \tag{5}$$

On an arbitrary stress state, it is assumed that:

$$\kappa_c=\varphi_c(\sigma_{ij})\kappa \quad \kappa_t=\varphi_t(\sigma_{ij})\kappa \tag{6}$$

Functions $\varphi_t(\sigma_{ij})$ and $\varphi_c(\sigma_{ij})$ should be chosen in such a way that, for loading processes with dominant tensile stress states, $\varphi_t(\sigma_{ij})=1$ and $\varphi_c(\sigma_{ij})=0$; similarly, for loading processes with dominant compressive stress states $\varphi_t(\sigma_{ij})=0$ and $\varphi_c(\sigma_{ij})=1$, and for loading processes with tensile-compressive stress states $0<\varphi_t(\sigma_{ij})<1$ and $0<\varphi_c(\sigma_{ij})<1$. These functions must satisfy the condition of $\varphi_t(\sigma_{ij})+\varphi_c(\sigma_{ij})=1$. Consequently, weight functions $\varphi_t(\sigma_{ij})$ and $\varphi_c(\sigma_{ij})$ can be achieved expediently.

Using such conditions, the yield function can be expressed as

$$F(\sigma_{ij},\kappa,\dot{\kappa}) = F(\sigma_{ij},\kappa_c,\dot{\kappa}_c,\kappa_t,\dot{\kappa}_t) = 0 \tag{7}$$

At the same time, the viscoplastic consistency condition must be satisfied so that:

$$\frac{\partial F}{\partial \sigma_{ij}} d\sigma_{ij} + \frac{\partial F}{\partial \kappa_c} d\kappa_c + \frac{\partial F}{\partial \dot{\kappa}_c} d\dot{\kappa}_c + \frac{\partial F}{\partial \kappa_t} d\kappa_t + \frac{\partial F}{\partial \dot{\kappa}_t} d\dot{\kappa}_t = 0 \tag{8}$$

The effects of κ_t and $\dot{\kappa}_t$ on f_t are assumed to be independent and the instantaneous tensile strength f_t is formulated in a very general way as follows

$$f_t = f_{ts} H_t(\kappa_t) R_t(\dot{\kappa}_t) \tag{9}$$

Similarly, the instantaneous compressive strength is computed as

$$f_c = f_{cs} H_c(\kappa_c) R_c(\dot{\kappa}_c) \tag{10}$$

where $H_t(\kappa_t)$, $R_t(\dot{\kappa}_t)$, $H_c(\kappa_c)$ and $R_c(\dot{\kappa}_c)$ are the assumption functions achieved by experiment. Here, κ is adopted as $\kappa = \bar{\varepsilon}^{VP} = \sqrt{2\varepsilon_{ij}^{vp}\varepsilon_{ij}^{vp}/3}$.

3.2 Consistency viscoplastic William-Warnke three-parameter model of concrete (xiao, 2010)

In this study, the yield surface function is assumed to be the same as the failure surface function of concrete so that the yield function of the William-Warnke three-parameter model can be expressed as

$$F(\sigma_m,\tau_m,\theta) = \frac{1}{\rho}\sigma_m + \frac{1}{r(\theta)}\tau_m - f_c = 0 \tag{11}$$

where two parameters ρ and $r(\theta)$ are chosen by three conditions: 1) uniaxial tensile strength f_t, 2) uniaxial compressive strength f_c, and 3) biaxial compressive strength $f_{bc} = k_{bc} f_c$.

Defining $m_{ij} = \dfrac{\partial F}{\partial \sigma_{ij}}$, one can achieve:

$$\begin{aligned} m_{ij} &= \frac{\partial F}{\partial \sigma_{ij}} = \frac{\partial F}{\partial \sigma_m}\cdot\frac{\partial \sigma_m}{\partial \sigma_{ij}} + \frac{\partial F}{\partial \tau_m}\cdot\frac{\partial \tau_m}{\partial \sigma_{ij}} + \frac{\partial F}{\partial r}\cdot\frac{\partial r}{\partial \sigma_{ij}} \\ &= \frac{1}{\rho}\cdot\frac{1}{3}\delta_{ij} + \frac{1}{r}\cdot\frac{1}{5\tau_m}s_{ij} - \frac{\tau_m}{r^2}\frac{\partial r}{\partial \sigma_{ij}} \end{aligned} \tag{12}$$

where $\delta_{ij} = \partial I_1 / \partial \sigma_{ij}$ and $s_{ij} = \partial J_2 / \partial \sigma_{ij}$.

For the sake of simplicity, defining $A = \dfrac{1}{3\rho}$, $B = \dfrac{1}{5r\tau_m}$ and $C = -\dfrac{\tau_m}{r^2}$ and substituting them into equation (11), one obtains:

$$m_{ij} = \frac{\partial F}{\partial \sigma_{ij}} = A\delta_{ij} + Bs_{ij} + C\frac{\partial r}{\partial \sigma_{ij}} = A\delta_{ij} + Bs_{ij} + C\frac{\partial r}{\partial \theta}\frac{\partial \theta}{\partial \sigma_{ij}} \tag{13}$$

Defining $r = \frac{u}{v}$ and taking the partial derivative with respect to the stress tensor σ_{ij}, one obtains:

$$\frac{\partial r}{\partial \theta} = \frac{\partial (u/v)}{\partial \theta} = \frac{v \cdot du/d\theta - u \cdot dv/d\theta}{v^2} = D \tag{14}$$

where

$$u = 2r_c(r_c^2 - r_t^2)\cos\theta + r_c(2r_t - r_c)[4(r_c^2 - r_t^2)\cos^2\theta + 5r_t^2 - 4r_c r_t]^{1/2}$$

$$v = 4(r_c^2 - r_t^2)\cos^2\theta + (r_c - 2r_t)^2$$

$$\frac{du}{d\theta} = 2r_c(r_t^2 - r_c^2)\sin\theta + \frac{4r_c(2r_t - r_c)(r_t^2 - r_c^2)\sin\theta\cos\theta}{[4(r_c^2 - r_t^2)\cos^2\theta + 5r_t^2 - 4r_c r_t]^{1/2}}$$

$$\frac{dv}{d\theta} = 8(r_t^2 - r_c^2)\sin\theta\cos\theta$$

According to the William-Warnke three-parameter model, the relationship between θ and σ_{ij} is given as follows:

$$\cos 3\theta = \frac{3\sqrt{3}}{2} \cdot \frac{J_3}{J_2^{3/2}} \tag{15}$$

By taking the partial derivative of equation (11) with respect to the stress tensor σ_{ij}, the following expression can be obtained as:

$$\begin{aligned} \frac{\partial \theta}{\partial \sigma_{ij}} &= \frac{\partial \theta}{\partial J_2}\frac{\partial J_2}{\partial \sigma_{ij}} + \frac{\partial \theta}{\partial J_3}\frac{\partial J_3}{\partial \sigma_{ij}} = \frac{3\sqrt{3}}{4\sin 3\theta} \cdot \frac{J_3}{J_2^{5/2}} \cdot \frac{\partial J_2}{\partial \sigma_{ij}} + \frac{-\sqrt{3}}{2\sin 3\theta} \cdot \frac{1}{J_2^{3/2}} \cdot \frac{\partial J_3}{\partial \sigma_{ij}} \\ &= \frac{3\sqrt{3}}{4\sin 3\theta} \cdot \frac{J_3}{J_2^{5/2}} \cdot s_{ij} - \frac{\sqrt{3}}{2\sin 3\theta} \cdot \frac{1}{J_2^{3/2}} \cdot t_{ij} \end{aligned} \tag{16}$$

where $t_{ij} = \frac{\partial J_3}{\partial \sigma_{ij}}$ and t_{ij} has the behavior such as:

$$(1)\ t_{ij}\delta_{ij} = 0 \qquad (2)\ t_{ij}s_{ij} = 3J_3 \qquad (3)\ t_{ij}t_{ij} = \frac{2}{3}J_2^2$$

Simply, defining $E=\frac{3\sqrt{3}}{4\sin 3\theta}\cdot\frac{J_3}{J_2^{5/2}}$ and $U=-\frac{\sqrt{3}}{2\sin 3\theta}\cdot\frac{1}{J_2^{3/2}}$, equation (16) can be expressed as

$$\frac{\partial\theta}{\partial\sigma_{ij}}=E\cdot s_{ij}+U\cdot t_{ij} \tag{17}$$

Substituting equations (10) and (13) into equation (9), m_{ij} is simplified as:

$$\begin{aligned} m_{ij}&=\frac{\partial F}{\partial\sigma_{ij}}=A\cdot\delta_{ij}+B\cdot s_{ij}+CD(E\cdot s_{ij}+U\cdot t_{ij})\\ &=A\cdot\delta_{ij}+(B+CDE)\cdot s_{ij}+CDU\cdot t_{ij}\\ &=\alpha\delta_{ij}+\beta s_{ij}+\gamma t_{ij}\end{aligned} \tag{18}$$

where $\alpha=A$, $\beta=B+CDE$ and $\gamma=CDU$.

In equation (5), $\frac{\partial F}{\partial\kappa_c}$, $\frac{\partial F}{\partial\dot{\kappa}_c}$, $\frac{\partial F}{\partial\kappa_t}$ and $\frac{\partial F}{\partial\dot{\kappa}_t}$ could be expressed as

$$\frac{\partial F}{\partial\kappa_c}=\frac{\partial F}{\partial f_c}\frac{\partial f_c}{\partial\kappa_c}=(\frac{\partial F}{\partial\rho}\frac{\partial\rho}{\partial f_c}+\frac{\partial F}{\partial r}\frac{\partial r}{\partial f_c})\frac{\partial f_c}{\partial\kappa_c}$$

$$\frac{\partial F}{\partial\dot{\kappa}_c}=\frac{\partial F}{\partial f_c}\frac{\partial f_c}{\partial\dot{\kappa}_c}=(\frac{\partial F}{\partial\rho}\frac{\partial\rho}{\partial f_c}+\frac{\partial F}{\partial r}\frac{\partial r}{\partial f_c})\frac{\partial f_c}{\partial\dot{\kappa}_c}$$

$$\frac{\partial F}{\partial\kappa_t}=\frac{\partial F}{\partial f_t}\frac{\partial f_t}{\partial\kappa_t}=(\frac{\partial F}{\partial\rho}\frac{\partial\rho}{\partial f_t}+\frac{\partial F}{\partial r}\frac{\partial r}{\partial f_t})\frac{\partial f_t}{\partial\kappa_t}$$

$$\frac{\partial F}{\partial\dot{\kappa}_t}=\frac{\partial F}{\partial f_t}\frac{\partial f_t}{\partial\dot{\kappa}_t}=(\frac{\partial F}{\partial\rho}\frac{\partial\rho}{\partial f_t}+\frac{\partial F}{\partial r}\frac{\partial r}{\partial f_t})\frac{\partial f_t}{\partial\dot{\kappa}_t}$$

where the curves of $\frac{\partial f_c}{\partial\kappa_c}$, $\frac{\partial f_c}{\partial\dot{\kappa}_c}$, $\frac{\partial f_t}{\partial\kappa_t}$ and $\frac{\partial f_t}{\partial\dot{\kappa}_t}$ can be achieved by uniaxial compressive and tensile tests of concrete.

Based on the associated plastic flow rule, the viscoplastic strain is defined as

$$d\varepsilon_{ij}^{vp}=d\lambda\frac{\partial F}{\partial\sigma_{ij}}=d\lambda m_{ij} \tag{19}$$

The invariable can be expressed as

$$d\kappa=\sqrt{\frac{2}{3}d\varepsilon_{ij}^{vp}d\varepsilon_{ij}^{vp}}=\sqrt{\frac{2}{3}m_{ij}m_{ij}}d\lambda=g(\sigma_{ij})d\lambda \tag{20}$$

Using these functions, the consistency equation (4) can be expressed as

$$m_{ij}d\sigma_{ij} + hd\lambda + sd\dot{\lambda} = 0 \tag{21}$$

where

$$h = \frac{\partial F}{\partial \lambda} = a_c h_c(\kappa_c) R_c(\dot{\kappa}_c) + a_t h_t(\kappa_t) R_t(\dot{\kappa}_t)$$

$$s = \frac{\partial F}{\partial \dot{\lambda}} = a_c H_c(\kappa_c) r_c(\dot{\kappa}_c) + a_t H_t(\kappa_t) r_t(\dot{\kappa}_t)$$

In which

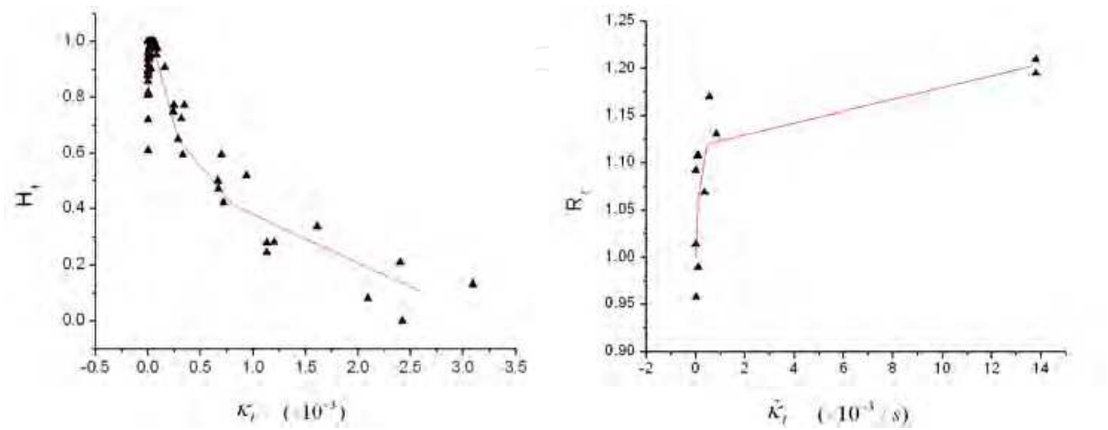
$$a_t = \frac{\partial F}{\partial f_t} f_{ts}\varphi_t(\sigma_{ij}) g(\sigma_{ij}) \quad a_c = \frac{\partial F}{\partial f_c} f_{cs}\varphi_c(\sigma_{ij}) g(\sigma_{ij})$$

$$h_t(\kappa_t) = \frac{\partial H_t(\kappa_t)}{\partial \kappa_t} \quad h_c(\kappa_c) = \frac{\partial H_c(\kappa_c)}{\partial \kappa_c}$$

$$r_t(\dot{\kappa}_t) = \frac{\partial R_t(\dot{\kappa}_t)}{\partial \dot{\kappa}_t} \quad r_c(\dot{\kappa}_c) = \frac{\partial R_c(\dot{\kappa}_c)}{\partial \dot{\kappa}_c}$$

Dynamic tensile and compressive tests were carried out to investigate the effect of strain rates on the dynamic tensile and compressive behaviors of concrete (Xiao, 2008). Test results indicate that the tensile and compressive strengths of concrete increase with the increase of the loading rate. The initial tangential modulus and the critical strain of concrete in tension are independent of strain rate, but those in compression slightly increased with the strain rate. Poisson's ratio of concrete in both tension and compression is not obviously dependent on loading rate.

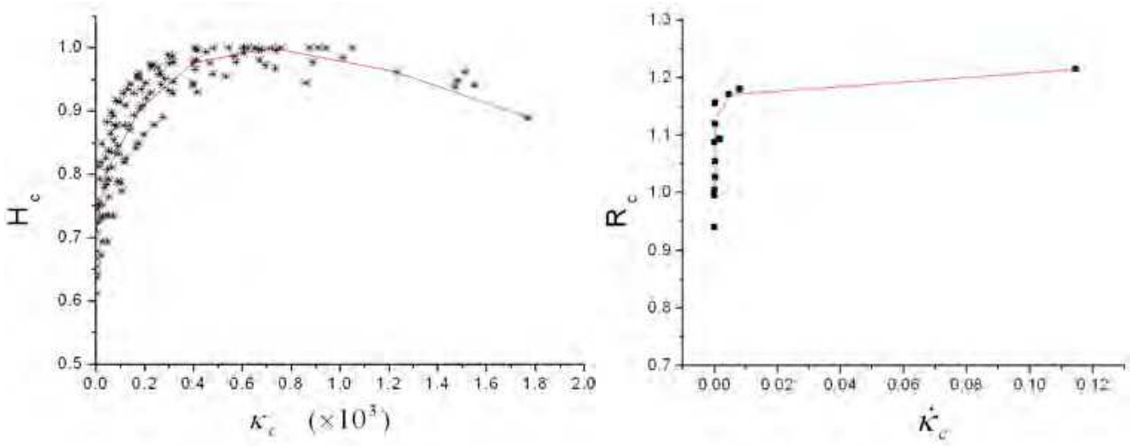
Based on the experimental data, the functions $H_t(\kappa_t)$ and $R_t(\dot{\kappa}_t)$ are given in **Fig. 9(a)** and **Fig. 9(b)**, where the plotted curves are the fitting curves for the later calculation.



(a) Function of $H_t(\kappa_t)$ (b) Function of $R_t(\dot{\kappa}_t)$

Fig. 9. Function of $H_t(\kappa_t)$ and $R_t(\dot{\kappa}_t)$

Similarly, the functions of $H_c(\kappa_c)$ and $R_c(\dot{\kappa}_c)$ are given in **Fig. 10(a)** and **Fig. 10(b)**.



(a) Function of $H_c(\kappa_c)$ (b) Function of $R_c(\dot{\kappa}_c)$

Fig. 10. Function of $H_c(\kappa_c)$ and $R_c(\dot{\kappa}_c)$

3.3 Euler return mapping algorithm

At the time t, the stress σ_{ij}^t, the invariable κ^t and the rate of invariable $\dot{\kappa}^t$ should satisfy the yield condition:

$$F(\sigma_{ij}^t, \kappa^t, \dot{\kappa}^t) = 0 \tag{22}$$

At the time $t + \Delta t$, the stress can be written as

$$\sigma_{ij}^{t+\Delta t} = \sigma_{ij}^t + \Delta\sigma_{ij} = \sigma_{ij}^t + D_{ijkl}^{ep}(\sigma_{ij}, \Delta\lambda)\Delta\varepsilon_{kl} \tag{23}$$

where $D_{ijkl}^{ep}(\sigma_{ij}, \Delta\lambda)$ is the tangent module of the consistency viscoplastic model.

Also, the stress $\sigma_{ij}^{t+\Delta t}$, the invariable $\kappa^{t+\Delta t}$ and the rate of invariable $\dot{\kappa}^{t+\Delta t}$ at the time $t + \Delta t$ should satisfy the yield condition:

$$F(\sigma_{ij}^{t+\Delta t}, \kappa^{t+\Delta t}, \dot{\kappa}^{t+\Delta t}) = 0 \tag{24}$$

At the short time increment, the assumption is an approximation for $\dot{\lambda}$ as

$$\dot{\lambda} = \frac{\lambda^{t+\Delta t}}{\Delta t} \tag{25}$$

Thus, the internal parameter $\kappa^{t+\Delta t}$ and its rate $\dot{\kappa}^{t+\Delta t}$ can be expressed by

$$\dot{\kappa}^{t+\Delta t} = \dot{\lambda}^{t+\Delta t} g(\sigma_{ij}^{t+\Delta t}) = \frac{\Delta\lambda^{t+\Delta t}}{\Delta t} g(\sigma_{ij}^{t+\Delta t}) \tag{26}$$

$$\kappa^{t+\Delta t} = \kappa^{t} + \Delta\lambda^{t+\Delta t} g(\sigma_{ij}^{t+\Delta t}) \tag{27}$$

Consequently, the yield condition at the time $t+\Delta t$ can be formulated using the above expression as in the classic rate-independent plasticity as follows:

$$F(\sigma_{ij}^{t+\Delta t}, \Delta\lambda^{t+\Delta t}) = 0 \tag{28}$$

During the kth iteration at the time $t+\Delta t$，the stress σ_{ij}^{k} and plastic multiplier $\Delta\lambda^{k}$ might not satisfy the yield condition:

$$F^{k}(\sigma_{ij}^{k}, \Delta\lambda^{k}) \neq 0 \tag{29}$$

Generally, the stress σ_{ij}^{k} does not reflect the real stress $\sigma_{ij}^{t+\Delta t}$ at the end of the given time $t+\Delta t$. So, the residual stress can be expressed as

$$r_{ij}^{k}(\sigma_{ij}^{k}, \Delta\lambda^{k}) = \sigma_{ij}^{k} - \sigma_{ij}^{t+\Delta t} = \sigma_{ij}^{k} - \sigma_{ij}^{t} - D_{ijkl}^{ep}(\sigma_{ij}, \Delta\lambda)\Delta\varepsilon_{kl} \tag{30}$$

During the $(k+1)$th iteration at the time $t+\Delta t$，the yield function value F^{k+1} and the residual stress r_{ij}^{k+1} can be achieved from the truncated Taylor's series expansion of the yield F and the residual stress r_{ij} about position k, and then set to zero:

$$F^{k+1} = F^{k} + \frac{\partial F^{k}}{\partial \sigma_{ij}}\delta\sigma_{ij}^{k} + \frac{\partial F^{k}}{\partial \Delta\lambda}\delta\Delta\lambda^{k} = 0 \tag{31}$$

$$r_{ij}^{k+1} = r_{ij}^{k} + \frac{\partial r^{k}}{\partial \sigma_{ij}}\delta\sigma_{ij}^{k} + \frac{\partial r^{k}}{\partial \Delta\lambda}\delta\Delta\lambda^{k} = 0 \tag{32}$$

Equations (31) and (32) represent a set of linear equations for the iterative stress update $\delta\sigma_{ij}^{k}$ and the iterative viscoplastic multiplier update $\delta\Delta\lambda^{k}$.

Defining

$$[\mathbf{A}] = \begin{bmatrix} \dfrac{\partial F^{k}}{\partial \Delta\lambda} & \dfrac{\partial F^{k}}{\partial \sigma_{ij}} \\ \dfrac{\partial r^{k}}{\partial \Delta\lambda} & \dfrac{\partial r^{k}}{\partial \sigma_{ij}} \end{bmatrix}$$

$$\{\mathbf{b}\} = \begin{Bmatrix} -F^{k} \\ -r_{ij}^{k} \end{Bmatrix}$$

equations (31) and (32) can be expressed as

$$[\mathbf{A}]\begin{Bmatrix}\delta\Delta\lambda^k\\ \delta\sigma_{ij}^k\end{Bmatrix}=\{\mathbf{b}\} \tag{33}$$

where

$$\frac{\partial F^k}{\partial\Delta\lambda}=\frac{\partial F^k}{\partial\lambda}+\frac{\partial F^k}{\partial\dot{\lambda}}\frac{d\dot{\lambda}}{d\Delta\lambda}=\frac{\partial F^k}{\partial\lambda}+\frac{\partial F^k}{\partial\dot{\lambda}}\frac{1}{\Delta t}=h^k+\frac{s^k}{\Delta t}$$

$$\frac{\partial F}{\partial\sigma_{ij}}=m_{ij}=\alpha\delta_{ij}+\beta s_{ij}+\gamma t_{ij}$$

$$\frac{\partial r}{\partial\Delta\lambda}=-\frac{\partial(D_{ijkl}^{ep}\Delta\varepsilon_{kl})}{\partial\Delta\lambda}$$

$$\frac{\partial r_{ij}}{\partial\sigma_{kl}}=I_{ijkl}-\frac{\partial}{\partial\sigma_{kl}}(D_{ijpq}^{ep}\Delta\varepsilon_{pq})$$

where I_{ijkl} was the identity tensor of the fourth order.

Taking into account the symmetry of the stress tensor, the iterative stress update $\delta\sigma_{ij}^k$ and the iterative viscoplastic multiplier update $\delta\Delta\lambda^k$ are achieved by solving the set of linear equations. The iteration process continues until the norms $|F|$ and $|r_{ij}|$ reaches to reasonably small ammount. The final values of $\Delta\lambda$ and $\Delta\sigma_{ij}$ at the end of the time step are obtained by a summation process:

$$\Delta\lambda=\sum_{k=1}^{N}\delta\Delta\lambda^k \tag{34}$$

$$\Delta\sigma_{ij}=\sum_{k=1}^{N}\delta\sigma_{ij}^k \tag{35}$$

where N is the total number of iterations.

3.4 Tangent module of the consistency viscoplastic model

According Hooke's law, the stress change can be written as

$$d\sigma_{ij}=D_{ijkl}^{e}d\varepsilon_{kl}^{e}=D_{ijkl}^{e}(d\varepsilon_{kl}-d\varepsilon_{kl}^{vp})=D_{ijkl}^{e}d\varepsilon_{kl}-D_{ijkl}^{e}d\varepsilon_{kl}^{vp} \tag{36}$$

Substituting the equation (36) into the equation (8), the consistency viscoplastic condition is expressed by

$$\frac{\partial F}{\partial\sigma_{ij}}(D_{ijkl}^{e}d\varepsilon_{kl}-D_{ijkl}^{e}d\varepsilon_{kl}^{vp})+\frac{\partial F}{\partial\kappa}d\kappa+\frac{\partial F}{\partial\dot{\kappa}}d\dot{\kappa}=0 \tag{37}$$

According to the flow law, the viscoplastic strain change is given by the following:

$$d\varepsilon_{ij}^{vp} = d\lambda \frac{\partial Q}{\partial \sigma_{ij}} \tag{38}$$

Substituting it into equation (37), one obtains

$$(\frac{\partial F}{\partial \sigma_{ij}}) D_{ijkl}^{e} d\varepsilon_{ij} - d\lambda (\frac{\partial F}{\partial \sigma_{ij}}) D_{ijkl}^{e} (\frac{\partial Q}{\partial \sigma_{ij}}) + \frac{\partial F}{\partial \kappa} d\kappa + \frac{\partial F}{\partial \dot{\kappa}} d\dot{\kappa} = 0 \tag{39}$$

Therefore, the viscoplastic multiplier is expressed as

$$d\lambda = \frac{(\frac{\partial F}{\partial \sigma_{ij}}) D_{ijkl}^{e} d\varepsilon_{ij}}{(\frac{\partial F}{\partial \sigma_{ij}}) D_{ijkl}^{e} (\frac{\partial Q}{\partial \sigma_{kl}}) - \frac{1}{d\lambda} \frac{\partial F}{\partial \kappa} d\kappa - \frac{1}{d\lambda} \frac{\partial F}{\partial \dot{\kappa}} d\dot{\kappa}} \tag{40}$$

Substituting it into equation (36), the following formula is obtained as

$$\begin{aligned} d\sigma_{ij} &= D_{ijkl}^{e} d\varepsilon_{kl} - D_{ijkl}^{e} d\varepsilon_{kl}^{vp} \\ &= D_{ijkl}^{e} d\varepsilon_{kl} - D_{ijkl}^{e} d\lambda \frac{\partial Q}{\partial \sigma_{kl}} \\ &= D_{ijkl}^{e} d\varepsilon_{kl} - D_{ijkl}^{e} \frac{\frac{\partial F}{\partial \sigma_{mn}} D_{mnpq}^{e} d\varepsilon_{pq}}{\frac{\partial F}{\partial \sigma_{mn}} D_{mnpq}^{e} \frac{\partial Q}{\partial \sigma_{pq}} - \frac{1}{d\lambda} \frac{\partial F}{\partial \kappa} d\kappa - \frac{1}{d\lambda} \frac{\partial F}{\partial \dot{\kappa}} d\dot{\kappa}} \frac{\partial Q}{\partial \sigma_{kl}} \\ &= D_{ijkl}^{e} d\varepsilon_{kl} - \frac{D_{ijkl}^{e} \frac{\partial F}{\partial \sigma_{mn}} D_{mnpq}^{e} \frac{\partial Q}{\partial \sigma_{kl}} \delta_{kp} \delta_{lq}}{\frac{\partial F}{\partial \sigma_{mn}} D_{mnpq}^{e} \frac{\partial Q}{\partial \sigma_{pq}} - \frac{1}{d\lambda} \frac{\partial F}{\partial \kappa} d\kappa - \frac{1}{d\lambda} \frac{\partial F}{\partial \dot{\kappa}} d\dot{\kappa}} d\varepsilon_{kl} \\ &= (D_{ijkl}^{e} + D_{ijkl}^{vp}) d\boldsymbol{\varepsilon}_{kl} = D_{ijkl}^{ep} d\varepsilon_{kl} \end{aligned} \tag{41}$$

where D_{ijkl}^{ep} is the tangent module of the consistency viscoplastic model.

$$\begin{aligned} D_{ijkl}^{ep} &= D_{ijkl}^{e} + D_{ijkl}^{vp} \\ &= D_{ijkl}^{e} - \frac{D_{ijkl}^{e} \frac{\partial F}{\partial \sigma_{mn}} D_{mnpq}^{e} \frac{\partial Q}{\partial \sigma_{kl}} \delta_{kp} \delta_{lq}}{\frac{\partial F}{\partial \sigma_{mn}} D_{mnpq}^{e} \frac{\partial Q}{\partial \sigma_{pq}} - \frac{1}{d\lambda} \frac{\partial F}{\partial \kappa} d\kappa - \frac{1}{d\lambda} \frac{\partial F}{\partial \dot{\kappa}} d\dot{\kappa}} \end{aligned} \tag{42}$$

Therefore,

$$D_{ijkl}^{vp} = -\frac{D_{ijkl}^{e}\frac{\partial F}{\partial \sigma_{mn}}D_{mnpq}^{e}\frac{\partial Q}{\partial \sigma_{kl}}\delta_{kp}\delta_{lq}}{\frac{\partial F}{\partial \sigma_{mn}}D_{mnpq}^{e}\frac{\partial Q}{\partial \sigma_{pq}} - \frac{1}{d\lambda}\frac{\partial F}{\partial \kappa}d\kappa - \frac{1}{d\lambda}\frac{\partial F}{\partial \dot{\kappa}}d\dot{\kappa}} \tag{43}$$

The yield function of the classic William-Warnke three-parameter model is expressed as

$$F(\sigma_m, \tau_m, \theta) = \frac{1}{\rho}\sigma_m + \frac{1}{r(\theta)}\tau_m - f_c = 0 \tag{44}$$

The divergence of the yield function is written as

$$\frac{\partial F}{\partial \sigma_{ij}} = \alpha\delta_{ij} + \beta s_{ij} + \gamma t_{ij} \tag{45}$$

To the relative flow criteria, the flow law is the same as the yield function of the model:

$$Q(\sigma_{ij}, \kappa, \dot{\kappa}) = F(\sigma_{ij}, \kappa, \dot{\kappa}) \tag{46}$$

Then, the tangent module of the consistency viscoplastic model can be written as follows

$$\begin{aligned} D_{ijkl}^{vp} &= -\frac{D_{ijkl}^{e}\frac{\partial F}{\partial \sigma_{mn}}D_{mnpq}^{e}\frac{\partial Q}{\partial \sigma_{kl}}\delta_{kp}\delta_{lq}}{\frac{\partial F}{\partial \sigma_{mn}}D_{mnpq}^{e}\frac{\partial Q}{\partial \sigma_{pq}} - \frac{1}{d\lambda}\frac{\partial F}{\partial \kappa}d\kappa - \frac{1}{d\lambda}\frac{\partial F}{\partial \dot{\kappa}}d\dot{\kappa}} \\ &= -\frac{D_{ijkl}^{e}(\alpha\delta_{mn} + \beta s_{mn} + \gamma t_{mn})D_{mnpq}^{e}(\alpha\delta_{kl} + \beta s_{kl} + \gamma t_{kl})\delta_{kp}\delta_{lq}}{(\alpha\delta_{mn} + \beta s_{mn} + \gamma t_{mn})D_{mnpq}^{e}(\alpha\delta_{pq} + \beta s_{pq} + \gamma t_{pq}) - h - \frac{s}{\Delta t}} \\ &= -\frac{(3K\alpha\delta_{ij} + 2G\beta s_{ij} + 2G\gamma t_{ij})(3K\alpha\delta_{kl} + 2G\beta s_{kl} + 2G\gamma t_{kl})}{9K\alpha^2 + 4G\beta^2 J_2 + \frac{4}{3}G\gamma^2 J_2^2 + 12G\beta\gamma J_3 - h - \frac{s}{\Delta t}} \end{aligned} \tag{47}$$

Defining

$$P_0 = \sqrt{9K\alpha^2 + 4G\beta^2 J_2 + \frac{4}{3}G\gamma^2 J_2^2 + 12G\beta\gamma J_3 - h - \frac{s}{\Delta t}}$$

$$P_1 = 3K\alpha / P_0$$

$$P_2 = 2G\beta / P_0$$

$$P_3 = 2G\gamma / P_0$$

Therefore, the equation (47) can be expressed as

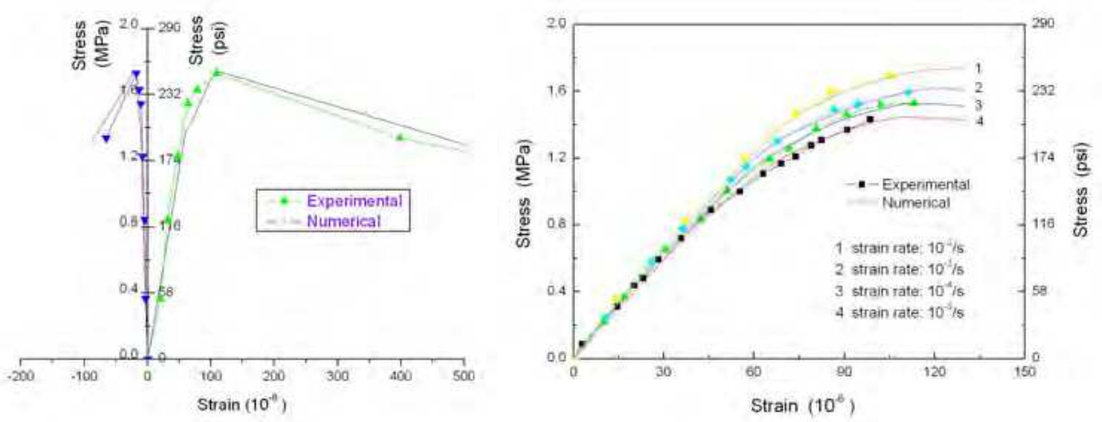
$$D_{ijkl}^{vp} = -(P_1\delta_{ij} + P_2 s_{ij} + P_3 t_{ij})(P_1\delta_{kl} + P_2 s_{kl} + P_3 t_{kl}) \tag{48}$$

The tangent module of the consistency viscoplastic model is obtained as

$$\begin{aligned} D_{ijkl}^{ep} &= D_{ijkl}^{e} + D_{ijkl}^{vp} \\ &= D_{ijkl}^{e} - (P_1\delta_{ij} + P_2 s_{ij} + P_3 t_{ij})(P_1\delta_{kl} + P_2 s_{kl} + P_3 t_{kl}) \end{aligned} \tag{49}$$

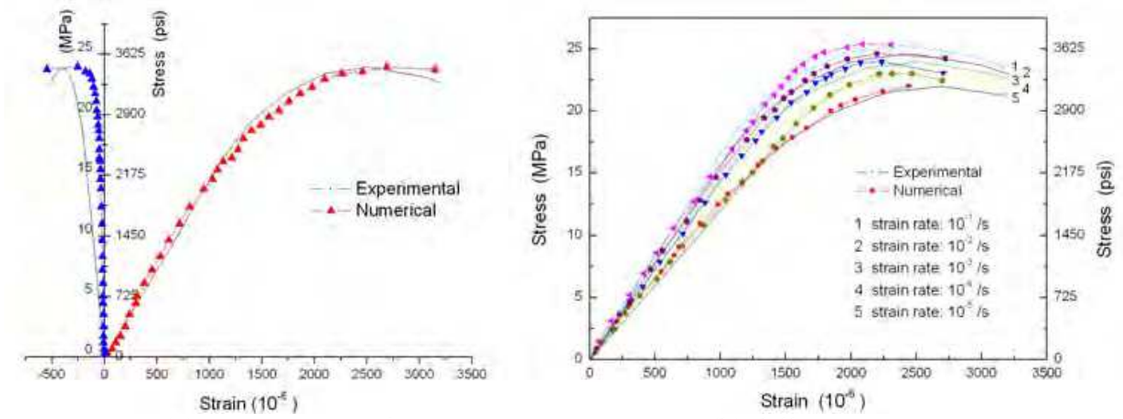
3.5 Comparisons with experimental data

The stress-strain curves of concrete for the uniaxial tension at the strain rate 10^{-3}/s, shown in **Fig. 11(a)**, are calculated and compared with experimental results. **Fig. 11(b)** shows the stress-strain curves of concrete for the uniaxial tension at the strain rate $10^{-5}s^{-1}$, $10^{-4}s^{-1}$, $10^{-3}s^{-1}$ and $10^{-2}s^{-1}$nd the comparisons with the experimental data. Similarly, the stress-strain curves of concrete for the uniaxial compression at the strain rate $10^{-2}s^{-1}$, shown in **Fig. 12(a)**, are calculated and compared with the experimental results. **Fig. 12(b)** illustrates the stress-strain curves of concrete for the uniaxial compression at the strain rate $110^{-5}s^{-1}$, $10^{-4}s^{-1}$, $10^{-3}s^{-1}$, $10^{-2}s^{-1}$ and $10^{-1}s^{-1}$ and the comparisons with the experimental data.



(a) strain rate 10^{-3}/s (b) different strain rates

Fig. 11. Model and tensile test results



(a) strain rate 10^{-2}/s (b) different strain rates

Fig. 12. Model and compressive test results

The consistency viscoplastic model is modified from the classic William-Warnke three-parameter model of concrete and has the advantages and disadvantages of the William-Warnke three-parameter model. It may directly simulate the dynamic behaviors of concrete and it is simple and easy to calculate. Thus, the proposed model is good for analyzing the dynamic responses of concrete structures.

3.6 Numerical example

In order to study the effect of strain rate on the dynamic response of concrete structures, the dynamic response of a simple-supporting beam with dimensions 8m×1m×1m is analyzed with this model. **Fig. 13** shows the discretized beam and calculated elements adopting three-dimension eight-node equivalent parameter elements. An impact loading is imposed on the midpoint of beam and **Fig. 14** depicts the loading history. Dynamic response is analyzed with the ADNFEM program compiled by the authors. The material properties are as follows: the elastic modulus of concrete is 1.6×10^4MPa, the Poisson's ratio is 0.17, the mass density is 2.4×10^3kg/m^3, the static compressive strength is 22MPa and the static tensile strength is 2.2MPa.

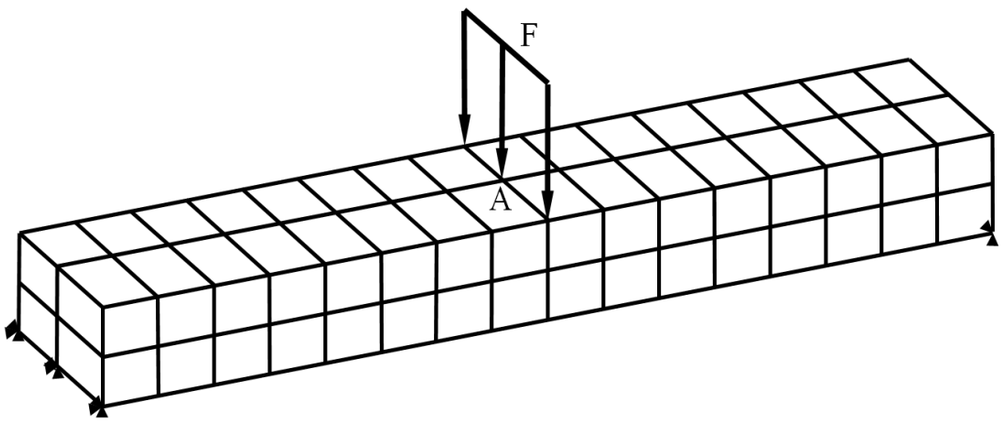


Fig. 13. Structure and meshes of the beam

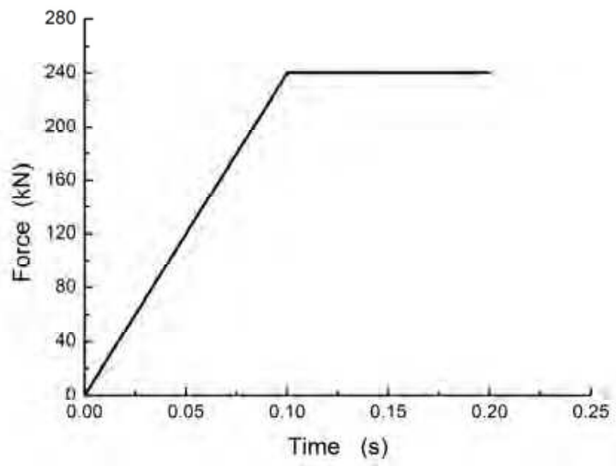


Fig. 14. Time-dependent curve of loading

Fig. 15 illustrates the displacement of midpoint A with time. Three curves shown in the figure denote the vertical displacement of the beam at model I (linear elastic model), model II (rate-dependent William-Warnke three-parameter model), and model III (rate-independent William-Warnke three-parameter model), respectively. **Fig. 15** shows that, at the beginning of loading, the beam is at the elastic state and three displacement curves are the same. When the stress of the beam reaches to the initial yield stress, the displacement curves of three models separate, and when time is 0.1 second, the loadings of three models reach to their maximums, but the displacements of the three models do not reach to their maximums at the same time. The vertical displacement of model I reaches to its maximum 1.50mm at time 0.114 second, but that of model II reaches to its maximum 1.62mm at time 0.110 second, and that of model III reaches to its maximum 1.90mm at time 0.117 second. It is clearly shown that displacement of the beam changes greatly after considering the effect of strain rate. The displacement of the beam with the model II decreases with 14.7 percent compared with that of the beam with model III but increases with 8.0 percent compared with that of the beam with model I.

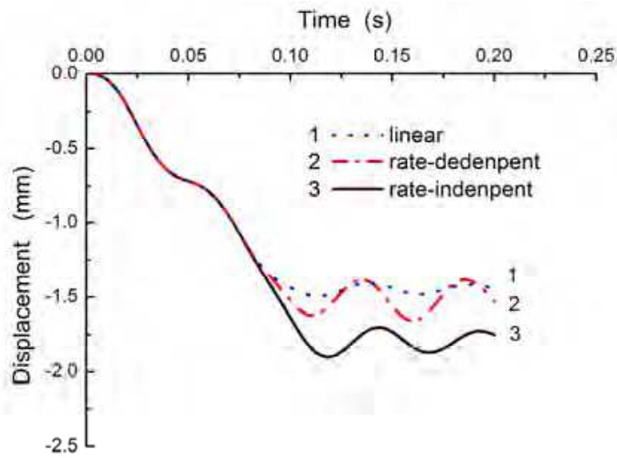


Fig. 15. Displacement of point A

At the same time, the stresses of the beam with the three models differ greatly from each other. **Table 7** lists the maximums of the tensile and compressive principal stress of the beam with the three models. It can be seen clearly that principal stresses of the beam with different models vary greatly. The tensile principal stress of the beam with model II increases with 13.10 percent compared with that of the beam with model III, but the compressive principal stress decreases with 11.6 percent. Compared with model I, the tensile principal stress of the beam with model II decreases with 16.80 percent, but the compressive principal stress increases with 19.1 percent. Similarly, the stress distribution of the beam changes greatly. **Fig. 16(a)**, **(b)** and **(c)** show the stress distribution of the beam with the three models respectively when the displacement is maximum. The tensile stress distribution figure is shown above and the compressive stress distribution figure is illustrated below. It can be seen clearly from these figures that the stress magnitudes and distributions of the beam change greatly with the different models. Consequently, it can be seen that the dynamic response of the concrete beam, the displacement, and the stress magnitude and distribution, change greatly after considering the effect of strain rate.

model	The first principal stress of point B MPa	The third principal stress of point A MPa
model I	1.97	-2.04
model II	1.64	-2.43
model III	1.45	-2.75

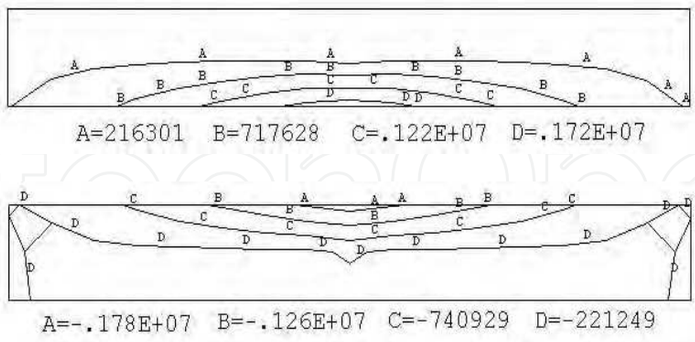
Table 7. Maximal principal stress of beam

4. Seismic response of arch dam

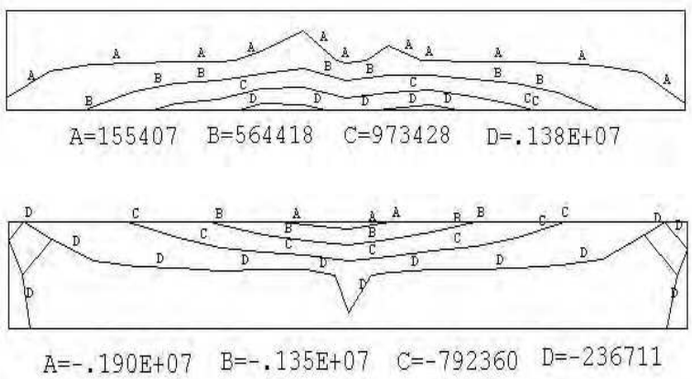
4.1 Model and parameters of arch dam

In order to illustrate the effect of the rate dependency on the dynamic structural response, a 278m high arch dam in China subjected to earthquake excitation is analyzed by the proposed model. The dam and the foundation are discretized into 450 and 1,040 three-dimensional isoparametric 8-node elements, respectively. **Fig. 17** shows the discretized dam-foundation system.

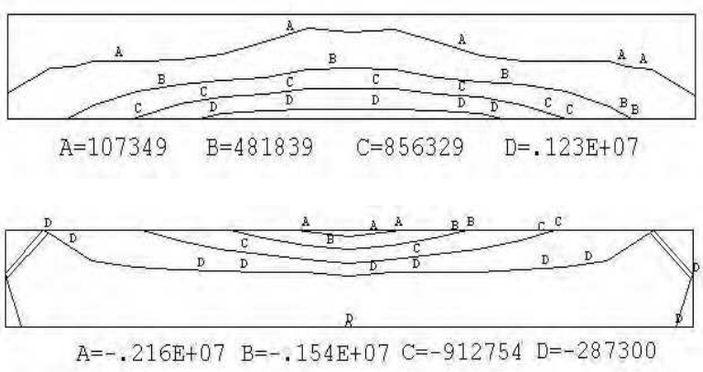
The material properties are as follows: for the dam body, the elastic module is 2.4×10^4MPa, the Poisson's ratio is 0.17, the density is 2.4×10^3kg/m^3, the static compressive strength is 30MPa, and the static tensile strength is 3MPa; for the foundation rock, the elastic module is 1.6×10^4MPa, the Poisson's ratio is 0.25, and the density is 2.0×10^3kg/m^3. The five lowest vibration frequencies of the dam in care of full reservoir are: f_1 =0.997Hz, f_2 =1.004Hz, f_3 =1.450Hz, f_4 =1.497Hz and f_5 =1.542Hz. An assumption of massless foundation is introduced to simplify the dam-foundation interaction analysis, although more rigorous interaction effects can be included.



(a) model I



(b) model II



(c) model III

Fig. 16. Distribution of principal stress of beam, Pa

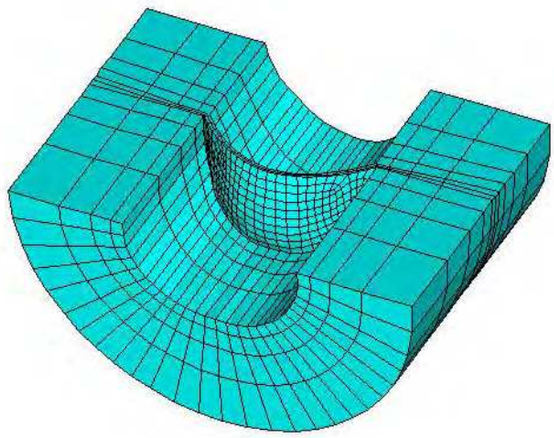


Fig. 17. Geometry and mesh of arch dam

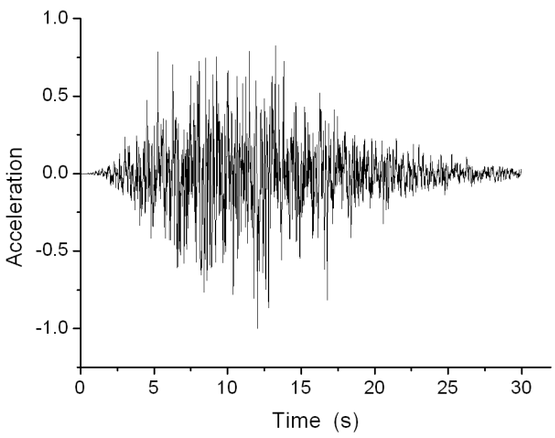


Fig. 18. Time history of earthquake input

Three-dimensional earthquake waves are used as the input. The design earthquake acceleration peak is 0.321 *gal* . **Fig. 18** shows the typical artificial unitary acceleragram that met the requirements of the Chinese Specifications for Seismic Design of Hydraulic Structures.

4.2 Design of the ADNFEM Program

The ADNFEM (Arch Dam Nonlinear Finite Element Method) program compiled by the authors is used to calculate the dynamic response of arch dams in the rate-dependent constitutive model. The program is validated by ANSYS in the rate-independent model when the strain rate was zero in the rate-dependent constitutive model.

The dynamic response of arch dams includes two parts: static analysis and seismic response analysis. The static analysis of arch dams is carried out to calculate the initial stress and strain state of the seismic response of arch dams. In order to form the Rayleigh damping matrix, the model of arch dams is calculated during the process of seismic response analysis. The processes of static analysis and seismic response analysis are listed as **Table 8** and **Table 9**.

1. Input initial data and form one-dimension bandwidth memory vector and constrain condition vector;
2. Input the constrain condition;
3. Set the loading step $I = 1$;
4. Form the Ith static load vector $\mathbf{f}$;
5. Judge elastic-plasticity state of every element and calculate the elastic-plasticity impact factor;
6. Form the tangent stiffness matrix of structures $\mathbf{K}$;
7. Calculate the elastic-plasticity predicted state;
8. Set the iterative $J = 1$ of the Ith loading step;
9. Solve for the iterative displacement $\delta\mathbf{u} = \mathbf{K}^{-1}\mathbf{f}$;
10. Update incremental displacements $\Delta\mathbf{u} = \Delta\mathbf{u} + \delta\mathbf{u}$;
11. For every Gaussian integration point:
    a. Compute the incremental strains $\Delta\boldsymbol{\varepsilon}$
    b. Compute the elastic-plastically predicted stress state $\boldsymbol{\sigma}^{ep} = \boldsymbol{\sigma}_t + \mathbf{D}^{ep}\Delta\boldsymbol{\varepsilon}$
    c. If $\boldsymbol{\sigma}^{ep}$ violates the yield criterion, perform the return mapping for the consistency model
12. Check for convergence, if not, *J*←*J+1*, go to step 9;
13. Update the loading step *I*←*I+1*, go to step 4;
14. Output the static analysis results.

Table 8. Summary of static analysis

1. Form the mass matrix $\mathbf{M}$ and initial stiffness matrix $\mathbf{K}$;
2. Calculate the first two frequencies ω_1 and ω_2 with the subspace iterative method;

Input structural damping ratio ξ and calculate the Rayleigh damping factor $\alpha_1 = \dfrac{2\omega_1\omega_2\xi}{\omega_1 + \omega_2}$, $\alpha_2 = \dfrac{2\xi}{\omega_1 + \omega_2}$;

3. Form the damping matrix $\mathbf{C} = \alpha_1\mathbf{M} + \alpha_2\mathbf{K}$;
4. Input the earthquake wave acceleration $\mathbf{a}_g$;
5. Initialize the parameters of the Newmark-β method β_N and γ_N;
6. Set the loading step $I = 1$;
7. Form the Ith earthquake load vector $\mathbf{f}_g^{t+\Delta t} = -\mathbf{M}\mathbf{a}_g^{t+\Delta t}$;
8. Initialize the displacements, velocities, and accelerations;

$$\Delta\mathbf{u} = 0\ ,\ \delta\mathbf{u} = 0\ ;$$

$$\mathbf{a}_{t+\Delta t}^{0} = -\frac{1}{\beta_N \Delta t}\mathbf{v}_t - (\frac{1}{2\beta_N} - 1)\mathbf{a}_t\ ,\ \mathbf{v}_{t+\Delta t}^{0} = (1 - \frac{\gamma_N}{\beta_N})\mathbf{v}_t + (1 - \frac{\gamma_N}{2\beta_N})\Delta t\mathbf{a}_t$$

9. Set the iterative $J=1$ of the Ith loading step;
10. Update velocities and accelerations

$$\mathbf{a}_{t+\Delta t}^{J}=\frac{1}{\beta_N \Delta t^2}\delta\mathbf{u}+\mathbf{a}_{t+\Delta t}^{J-1},\ \mathbf{v}_{t+\Delta t}^{J}=\frac{1}{\beta_N \Delta t}\delta\mathbf{u}+\mathbf{v}_{t+\Delta t}^{J-1};$$

11. Judge elastic-plasticity state of every element and calculate the elastic-plasticity impact factor;
12. Form the tangent stiffness matrix of structures $\mathbf{K}$;
13. Compute the equivalent stiffness matrix and equivalent force vector;

$$\bar{\mathbf{K}}=\mathbf{K}+\frac{1}{\beta_N \Delta t^2}\mathbf{M}+\frac{\gamma_N}{\beta_N \Delta t}\mathbf{C};$$

$$\bar{\mathbf{f}}=\mathbf{f}_g^t+\mathbf{M}\left(\frac{1}{\beta_N \Delta t}\mathbf{v}_{t+\Delta t}^{J}+\frac{1}{2\beta_N}\mathbf{a}_{t+\Delta t}^{J}\right)+\mathbf{C}\left\{\frac{\gamma_N}{\beta_N}\mathbf{v}_{t+\Delta t}^{J}+\left(\frac{\gamma_N}{2\beta_N}-1\right)\mathbf{a}_{t+\Delta t}^{J}\right\};$$

14. Solve for the iterative displacement $\delta\mathbf{u}=\bar{\mathbf{K}}^{-1}\bar{\mathbf{f}}$;
15. Update incremental displacements $\Delta\mathbf{u}=\Delta\mathbf{u}+\delta\mathbf{u}$;
16. For every Gaussian integration point:

a. Compute the incremental strains $\Delta\boldsymbol{\varepsilon}$

b. Compute the elastic-plastically predicted stress state $\boldsymbol{\sigma}^{ep}=\boldsymbol{\sigma}_t+\mathbf{D}^{ep}\Delta\boldsymbol{\varepsilon}$

c. If $\boldsymbol{\sigma}^{ep}$ violates the yield criterion, perform the return mapping for the consistency model

17. Check for convergence, if not, *J*←*J+1*, go to step 11;
18. Update the loading step *I*←*I+1*, go to step 8;
19. Output the seismic response analysis results.

Table 9. Summary of dynamic analysis

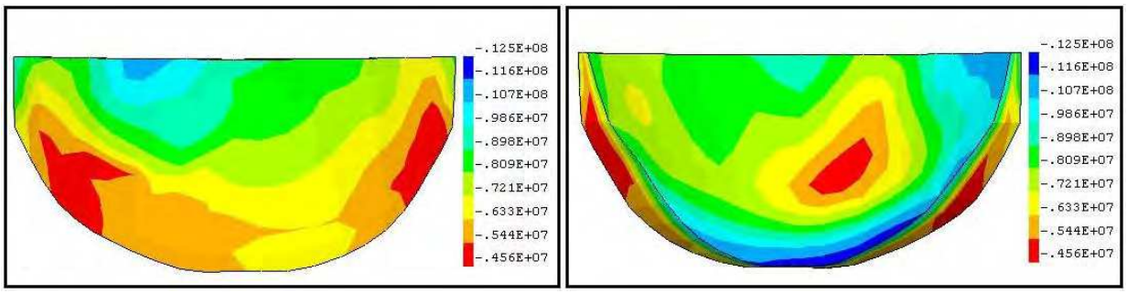
4.3 Seismic response of arch dam

4.3.1 Stresses in arch dams

The dynamic response analyses of the arch dam are performed with three models: model I (linear elastic model), model II (rate-dependent William-Warnke three-parameter model), and model III (rate-independent William-Warnke three-parameter model). The maximum values of the first and the third principle stresses in the dam are shown in **Table 10**. **Fig. 19** shows the distributions of the third principle stresses obtained from the three models. It is seen that, in all three cases, the maximum compressive stress is the same and appeared at the bottom of the upstream face; the material remaines working in the elastic range. While, for the maximum tensile stress there is the marked difference among the calculated results of the three models. Owing to the plasticity of concrete, the maximal values of the first principal stresses of model II and III decrease with 37.7% and 44.5%, respectively, compared with model I. Because the dynamic tensile strength of concrete increases with the increase of strain rates, the maximal values of the first principal stresses of model II, taking into account the effect of strain rates, increase with 12.2% compared with model III. **Fig. 20**, **Fig. 21** and **Fig. 22** show the distributions of the first principle stress obtained from the three models.

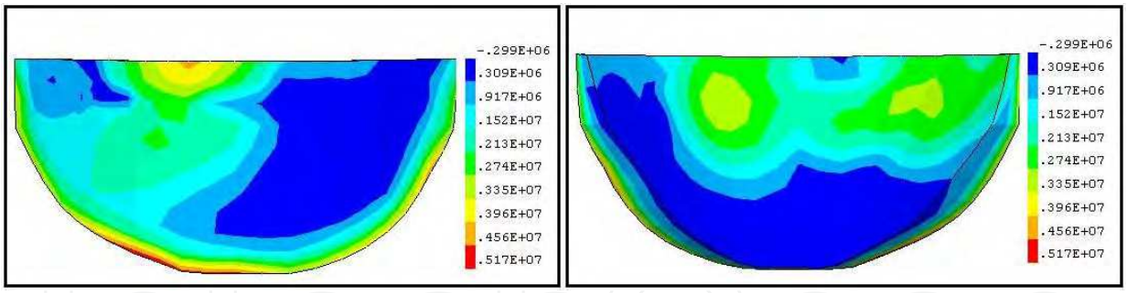
model	The first principal stress MPa	The third principal stress MPa
model I	5.17	-12.50
model II	3.22	-12.50
model III	2.87	-12.50

Table 10. Maximal principal stress of arch dam



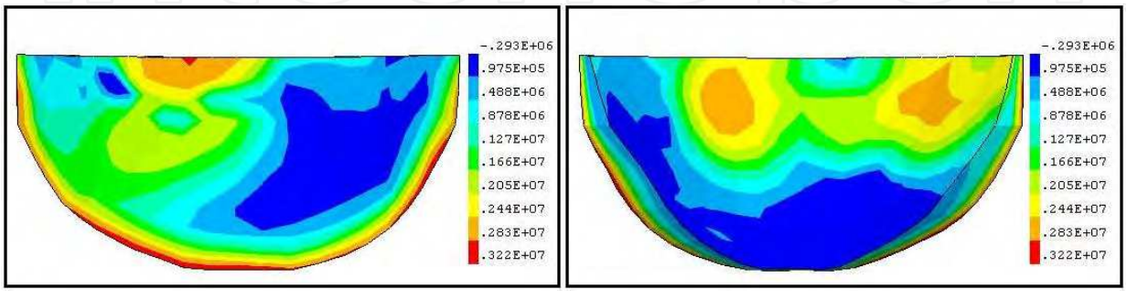
(a) upstream face (b) downstream face

Fig. 19. Distribution of the third principle stress (model I, II, and III), Mpa



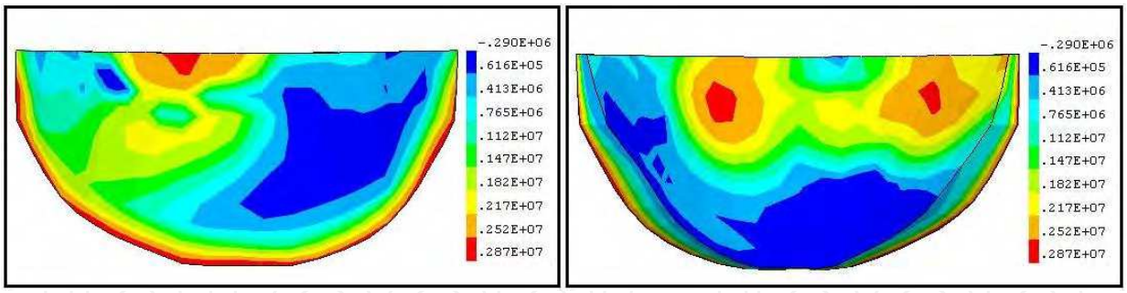
(a) upstream face (b) downstream face

Fig. 20. Distribution of the first principle stress (model I), Mpa



(a) upstream face (b) downstream face

Fig. 21. Distribution of the first principle stresses (model II), Mpa

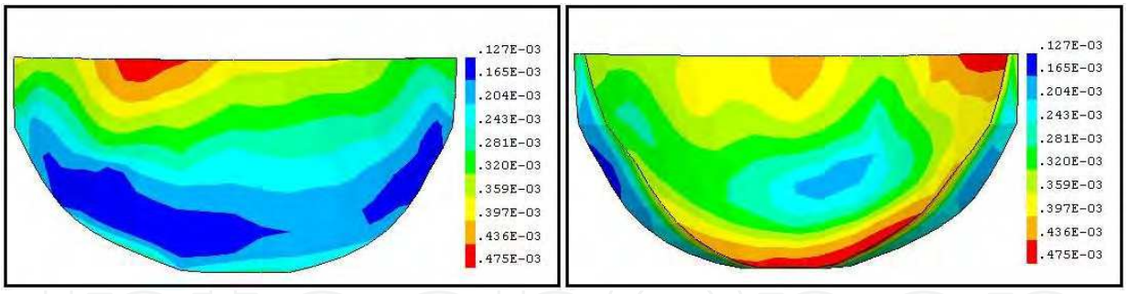


(a) upstream face (b) downstream face

Fig. 22. Distribution of the first principle stresses (model III), MPa

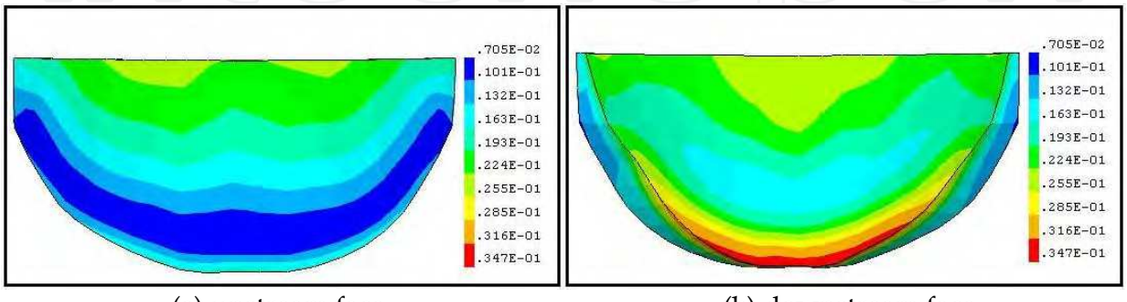
4.3.2 Strain and strain rate of arch dam

The maximal equivalent strain of concrete in three cases are the same because the compressive strain of concrete plays a more important role in the equivalent strain of concrete in the dominant compressive stress states, although the tensile strain is important in the dominant tensile stress states, but the values are smaller than those for the compressive strain. **Fig. 23** shows the distributions of the equivalent strain of the arch dam from the three models. It is clear that the maximal equivalent strain is 4.75×10^{-4}, and it appears at the bottom of the downstream face. Similarly, the maximal equivalent strain rates in the three cases are the same, and **Fig. 24** shows the distributions of the equivalent strain rates of the arch dam from the three models. The maximal equivalent strain rate is up to $3.47\times10^{-2}s^{-1}$ and it also appears at the bottom of the downstream face.



(a) upstream face (b) downstream face

Fig. 23. Distribution of the equivalent strain (model I, II, and III)

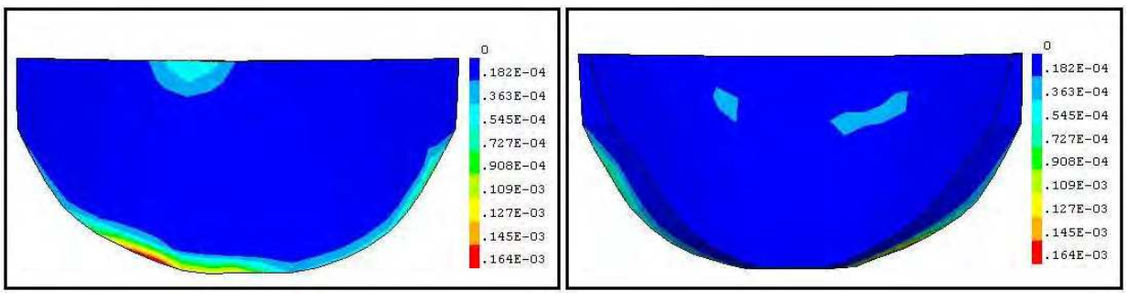


(a) upstream face (b) downstream face

Fig. 24. Distribution of the equivalent strain rate (model I, II, and III), s^{-1}

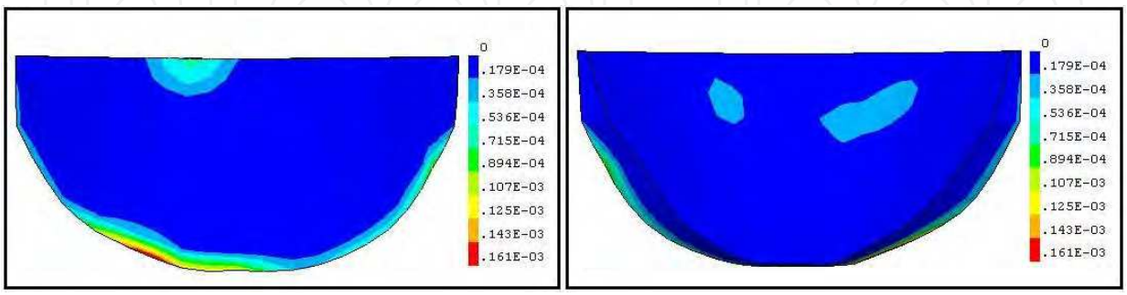
4.3.3 Plastic strain and plastic strain rate of arch dam

The equivalent viscoplastic strain of concrete appears only on the tensile zones of the arch dam. **Fig. 25** and **Fig. 26** show the distributions of the maximal equivalent viscoplastic strains obtained from model II and model III, respectively. It is shown that the maximal equivalent viscoplastic strains appear on the bottom of the upstream face and that the strain rates has little effect. **Fig.27** and **Fig.28** show the distributions of the maximal equivalent viscoplastic strain rates obtained from model II and model III, respectively. Similarly, the maximal equivalent viscoplastic strain rate appears on the bottom of the upstream face but it decreases with 17.5% after taking into account the effect of strain rates.



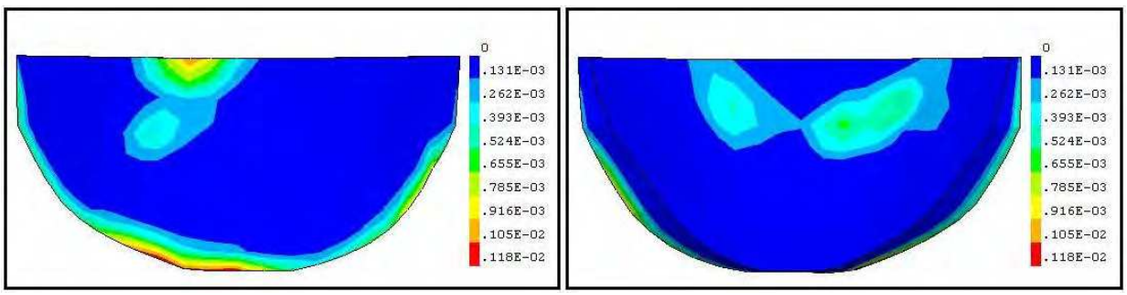
(a) upstream face (b) downstream face

Fig. 25. Distribution of the equivalent viscoplastic strain (model II)



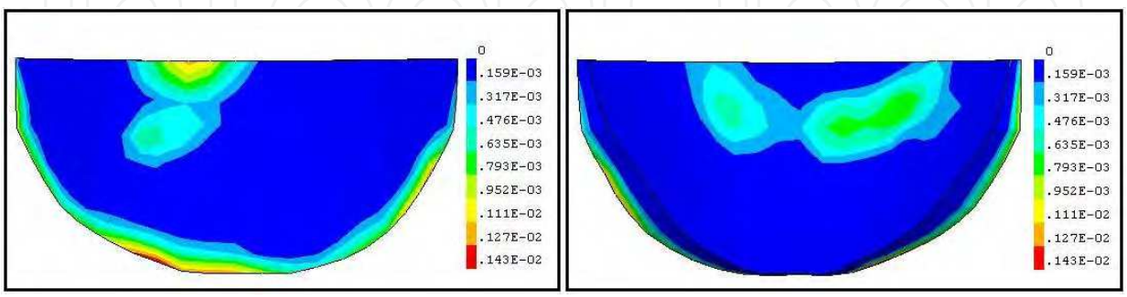
(a) upstream face (b) downstream face

Fig. 26. Distribution of the equivalent viscoplastic strain (model III)



(a) upstream face (b) downstream face

Fig. 27. Distribution of the equivalent viscoplastic strain rate (model II), s^{-1}



(a) upstream face (b) downstream face

Fig. 28. Distribution of the equivalent viscoplastic strain

5. Conclusions

Based on the numerical results obtained, the following conclusions are drawn:

1. Results indicate that the tensile and compressive strengths of concrete increase with increase of the rate of loading. The initial tangent modulus and the critical strain of concrete are independent of strain rate in tension but slightly increased as the strain rate increased in compression. Poisson's ratio of concrete isn't obviously dependent on the loading rate both in tension and in compression.
2. Comparisons between the models and experimental data show that the consistency model may simulate directly the uniaxial dynamic behaviors of concrete. The dynamic responses of a simple-supporting beam show that dynamic responses of concrete beam, the displacement, the stress magnitude and distribution, change greatly after considering the effect of strain rate.
3. In all three cases, the maximum values of the compressive stress are the same and the concrete remains working in the elastic range. The maximal values of the first principal stresses of the arch dam, taking into account the effect of strain rates, increase with 12.2% because the dynamic tensile strength of concrete increases with the increase of strain rates. There are no effects of strain rates on the maximal equivalent strain and the maximal equivalent strain rate of the arch dam. The strain rates have little effect on the maximal equivalent viscoplastic strain, while the maximal equivalent viscoplastic strain rate decreases with 17.5% after taking into account the effect of strain rates.

6. Acknowledgements

This study was founded by the National Science Foundation of China under grant No.50408030 and No. 51121005, the College Innovation Group of Liaoning Province under grant No: 2008T223 and the Fundamental Research Funds for the Central Universities under grant No: DUT10LK29.

7. Symbol notation

Symbol	Description
f_t	dynamic tensile strength of concrete
f_{ts}	static tensile strength of concrete
f_c	dynamic compressive strength of concrete
f_{ts}	static compressive strength of concrete
$\dot{\varepsilon}_t$	dynamic tensile strain rate
$\dot{\varepsilon}_{ts}$	quasi-static tensile strain rate
$\dot{\varepsilon}_c$	dynamic compressive strain rate
$\dot{\varepsilon}_{cs}$	quasi-static compressive strain rate
E	elastic modulus of concrete
K	volume module of concrete
G	shear module of concrete
μ	Poisson's ratio of concrete

σ_{ij}	the stress tensor
s_{ij}	the deviatoric stress tensor
r_{ij}	the residual stress tensor
σ_m	the average stress
τ_m	the average shear stress
ε_{ij}	the strain tensor
ε_{ij}^{vp}	the viscoplastic strain tensor
κ	internal variable
$\dot{\kappa}$	rate of internal variable
λ	the viscoplastic multiplier
φ_t	weight function of tensile invariable
φ_c	weight function of compressive invariable
F	yield function
Q	plastic flow function
I_1	the first invariant of stress tensor
J_2	the second invariant of deviatoric stress tensor
J_3	the third invariant of deviatoric stress tensor
D_{ijkl}^{e}	elastic stiffness of concrete
D_{ijkl}^{vp}	viscoplastic stiffness of concrete

8. References

Abrams DA (1917), "Effect of Rate of Application of Load on the Compressive Strength of Concrete," *ASTM Journal,* 17: 364-377.

Atchley BL and Furr HL (1967), "Strength and Energy-absorption Capabilities of Plain Concrete under Dynamic and Static Loading," *ACI Journal,* 64: 745-756.

Bai WF, Chen JY and Zhong H (2006), "Seismic Overload Response Analysis of Concrete Gravity Dam Based on Strain Rate-dependent Damage Model," *Journal of Hydraulic Engineering,* 37(7): 820-826. (in Chinese)

Birkimer DL and Lindemann R (1971), "Dynamic Tensile Strength of Concrete Materials," *ACI Journal Proceedings,* 1: 47-49.

Bischoff PH and Perry SH (1991), "Compressive Behaviour of Concrete at High Strain Rates," *Materials and Structures,* 24(144): 425-450.

Cadoni E, Labibes K and Albertini C (2001), "Strain-rate Effect on the Tensile Behaviour of Concrete at Different Relative Humidity Levels," *Materials and Structures,* 34(235): 21-26.

Cervera M, Oliver J and Manzoli O (1996), "A Rate-dependent Isotropic Damage Model for the Seismic Analysis of Concrete Dams," *Earthquake Engineering and Structural Dynamics,* 25: 987-1010.

Chen JY, Hu ZQ and Lin G (2004), "Seismic Analysis of Arch Dam with Joints Based on a New Strain-rate-dependant Plastic Damage Model," *Chinese Journal of Computational Mechanics,* 21(1): 45-49. (in Chinese)

Chinese Standard (2001), *Specifications for Seismic Design of Hydraulic Structures,* Beijing: Chinese Electric Power Press. (in Chinese)

Dhir RK and Sangha CM (1972), "A Study of Relationships between Time, Strength, Deformation and Fracture of Plain Concrete," *Magazine of Concrete Research,* 24(81): 197-208.

Dilger WH, Koch R and Kowalczyk R (1984), "Ductility of Plain and Confined Concrete under Different Strain Rates," *ACI Journal,* 81(1): 73-81.

Evans RH (1942), "Effect of Rate of Loading on the Mechanical Properties of Some Materials," *Journal of Institute of Civil Engineers,* 18(7-8): 96-306.

Harris DW, Mohorovic CE and Dolen TP (2000), "Dynamic Properties of Mass Concrete Obtained from Dam Cores," *ACI Material Journal,* 97(3): 290-296.

Hughes BP and Gregory R (1972), "Concrete Subjected to High Rates of Loading in Compression," *Magazine of Concrete Research,* 24(78): 25-36.

Jones PG and Richart FE (1936), "The Effect of Testing Speed on Strength and Elastic Properties of Concrete," *ASTM Journal,* 36: 380-392.

Lee J and Fenves GL (1998), "A Plastic-damage Concrete Model for Earthquake Analysis of Dams," *Earthquake Engineering and Structural Dynamics,* 27(9): 937-956.

Li J, Chen JY and Bai WF (2005), "Application of Strain Rate-dependent Damage Model in Analysis of Dynamic Opening of High Arch Dam Transverse Joints," *Journal of Hydraulic Engineering,* 36(7): 870-875. (in Chinese)

Malvar LJ and Ross CA (1998), "Review of Strain Rate Effects for Concrete in Tension," *ACI Materials Journal,* 95(6): 735-739.

Moore OL (1934), "Report of Working Committee of Committee C-1 on Plastic Mortar Tests for Portland Cement," *Proceedings of the American Society for Testing Materials,* 34: 322.

Norris CH, Hansen RJ, Holley MJ, Biggs JM, Namyet S and Minami JK (1959), *Structural Design for Dynamic Loads,* New York: McGraw-Hill Book Co. Inc.

Oh BH (1987), "Behavior of Concrete under Dynamic Tensile Loads," *ACI Materials Journal,* 84(1): 8-13.

Raphael JM (1984), "Tensile Strength of Concrete," *ACI Journal,* 87(17): 158-165.

Rossi P and Toutlemonde F (1996), "Effect of Loading Rate on the Tensile Behaviour of Concrete: Description of the Physical Mechanisms," *Materials and Structures,* 29(186): 116-118.

Rossi P, Van M and Jan GM (1994), "Effect of Loading Rate on the Strength of Concrete Subjected to Uniaxial Tension," *Materials and Structures,* 27(169): 260-264.

Rush H (1960), "Research towards a General Flexural Theory for Structural Concrete," *ACI Journal,* 57(1): 1-28.

Spark PR and Menzies JB (1973), "The Effect of Rate Loading upon the Static and Fatigue Strengths of Plain Concrete in Compression," *Magazine of Concrete Research,* 25(83): 83-80.

Spooner DC (1972), "Stress-stress-time Relationships for Concrete," *Magazine of Concrete Research,* 24(81): 197-208.

Tedesco JW, Ross CA, McGill PB and O'Neil BP (1991), "Numerical Analysis of High Strain-rate Concrete Direct Tension Tests," *Computers and Structures,* 40(2): 313-327.

Wang W (1997), *Stationary and Propagative Instabilities in Metals – a Computational Point of View,* PhD dissertation, TU Delft, Netherlands.

Watstein D (1953), "Effect of Straining Rate on the Compressive Strength and Elastic Properties of Concrete," *ACI Journal,* 49: 729-744.

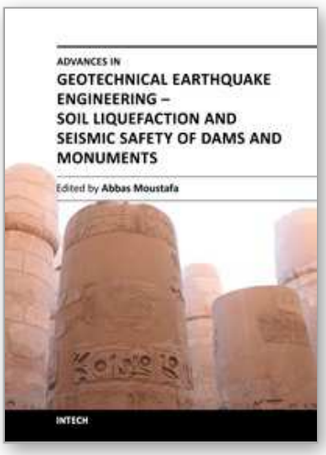
Winnicke A, Pearce CJ and Bicanic N (2001), "Viscoplastic Hoffman Consistency Model for Concrete," *Computers and Structures,* 79(1): 7-19.

Xiao SY, Li HN and Lin G (2008), "Dynamic Behaviour and Constitutive Model of Concrete at Different Strain Rates," *Magazine of Concrete Research,* 60(4): 271-278.

Xiao SY, Li HN and Lin G (2010), "3-D Consistency Dynamic Constitutive Model of Concrete," *Earthquake Engineering and Engineering Vibration*, 9(2): 233- 246.

Zielinski AJ, Reinhardt HW and Körmeling HA (1981), "Experiments on Concrete under Uniaxial Impact Tensile Loading," *Materials and Structures,* 14(80): 103-112.

IntechOpen



Advances in Geotechnical Earthquake Engineering - Soil Liquefaction and Seismic Safety of Dams and Monuments

Edited by Prof. Abbas Moustafa

ISBN 978-953-51-0025-6
Hard cover, 424 pages
Publisher InTech
Published online 10, February, 2012
Published in print edition February, 2012

This book sheds lights on recent advances in Geotechnical Earthquake Engineering with special emphasis on soil liquefaction, soil-structure interaction, seismic safety of dams and underground monuments, mitigation strategies against landslide and fire whirlwind resulting from earthquakes and vibration of a layered rotating plant and Bryan's effect. The book contains sixteen chapters covering several interesting research topics written by researchers and experts from several countries. The research reported in this book is useful to graduate students and researchers working in the fields of structural and earthquake engineering. The book will also be of considerable help to civil engineers working on construction and repair of engineering structures, such as buildings, roads, dams and monuments.

How to reference

In order to correctly reference this scholarly work, feel free to copy and paste the following:

Xiao Shiyun (2012). Rate-Dependent Nonlinear Seismic Response Analysis of Concrete Arch Dam, Advances in Geotechnical Earthquake Engineering - Soil Liquefaction and Seismic Safety of Dams and Monuments, Prof. Abbas Moustafa (Ed.), ISBN: 978-953-51-0025-6, InTech, Available from: http://www.intechopen.com/books/advances-in-geotechnical-earthquake-engineering-soil-liquefaction-and-seismic-safety-of-dams-and-monuments/rate-dependent-nonlinear-seismic-response-analysis-of-arch-dam

INTECH
open science | open minds

InTech Europe
University Campus STeP Ri
Slavka Krautzeka 83/A
51000 Rijeka, Croatia
Phone: +385 (51) 770 447
Fax: +385 (51) 686 166
www.intechopen.com

InTech China
Unit 405, Office Block, Hotel Equatorial Shanghai
No.65, Yan An Road (West), Shanghai, 200040, China
中国上海市延安西路65号上海国际贵都大饭店办公楼405单元
Phone: +86-21-62489820
Fax: +86-21-62489821

© 2012 The Author(s). Licensee IntechOpen. This is an open access article distributed under the terms of the Creative Commons Attribution 3.0 License, which permits unrestricted use, distribution, and reproduction in any medium, provided the original work is properly cited.

IntechOpen

IntechOpen